



AFRL-RB-WP-TR-2008-3170

**UNIQUE STEALTH UNMANNED AERIAL VEHICLE
(UAV) HOUCK AIRCRAFT DESIGN PROGRAM
Volume 1: Program Overview**

Aaron Altman

University of Dayton

**NOVEMBER 2008
Final Report**

Approved for public release; distribution unlimited.

See additional restrictions described on inside pages

STINFO COPY

**AIR FORCE RESEARCH LABORATORY
AIR VEHICLES DIRECTORATE
WRIGHT-PATTERSON AIR FORCE BASE, OH 45433-7542
AIR FORCE MATERIEL COMMAND
UNITED STATES AIR FORCE**

NOTICE

Using Government drawings, specifications, or other data included in this document for any purpose other than Government procurement does not in any way obligate the U.S. Government. The fact that the Government formulated or supplied the drawings, specifications, or other data does not license the holder or any other person or corporation; or convey any rights or permission to manufacture, use, or sell any patented invention that may relate to them.

This report was cleared for public release by the Air Force Research Laboratory Wright-Patterson Air Force Base (WPAFB) Public Affairs Office and is available to the general public, including foreign nationals. Copies may be obtained from the Defense Technical Information Center (DTIC) (<http://www.dtic.mil>).

AFRL-RB-WP-TR-2008-3170 HAS BEEN REVIEWED AND IS APPROVED FOR PUBLICATION IN ACCORDANCE WITH THE ASSIGNED DISTRIBUTION STATEMENT.

//signature//

CALE H. ZEUNE
Aerospace Engineer
Aerodynamic Configuration Branch
Aeronautical Sciences Division

//signature//

CHRISTOPHER P. GREEK
Chief
Aerodynamic Configuration Branch
Aeronautical Sciences Division

//signature//

DR. CARL TILMANN
Technical Advisor
Aerodynamic Configuration Branch
Aeronautical Sciences Division

This report is published in the interest of scientific and technical information exchange and its publication does not constitute the Government's approval or disapproval of its ideas or findings.

*Disseminated copies will show “//signature//” stamped or typed above the signature blocks.

REPORT DOCUMENTATION PAGE				<i>Form Approved</i> <i>OMB No. 0704-0188</i>	
The public reporting burden for this collection of information is estimated to average 1 hour per response, including the time for reviewing instructions, searching existing data sources, gathering and maintaining the data needed, and completing and reviewing the collection of information. Send comments regarding this burden estimate or any other aspect of this collection of information, including suggestions for reducing this burden, to Department of Defense, Washington Headquarters Services, Directorate for Information Operations and Reports (0704-0188), 1215 Jefferson Davis Highway, Suite 1204, Arlington, VA 22202-4302. Respondents should be aware that notwithstanding any other provision of law, no person shall be subject to any penalty for failing to comply with a collection of information if it does not display a currently valid OMB control number. PLEASE DO NOT RETURN YOUR FORM TO THE ABOVE ADDRESS.					
1. REPORT DATE (DD-MM-YY) November 2008		2. REPORT TYPE Final		3. DATES COVERED (From - To) 01 January 2006 – 01 May 2008	
4. TITLE AND SUBTITLE UNIQUE STEALTH UNMANNED AERIAL VEHICLE (UAV) HOUCK AIRCRAFT DESIGN PROGRAM Volume 1: Program Overview				5a. CONTRACT NUMBER FA8652-05-3-9017	
				5b. GRANT NUMBER	
				5c. PROGRAM ELEMENT NUMBER 0602201	
6. AUTHOR(S) Aaron Altman				5d. PROJECT NUMBER A0AA	
				5e. TASK NUMBER	
				5f. WORK UNIT NUMBER 0A	
7. PERFORMING ORGANIZATION NAME(S) AND ADDRESS(ES) University of Dayton 300 College Park Dayton, OH 45469-0210				8. PERFORMING ORGANIZATION REPORT NUMBER	
9. SPONSORING/MONITORING AGENCY NAME(S) AND ADDRESS(ES) Air Force Research Laboratory Air Vehicles Directorate Wright-Patterson Air Force Base, OH 45433-7542 Air Force Materiel Command United States Air Force				10. SPONSORING/MONITORING AGENCY ACRONYM(S) AFRL/RBAA	
				11. SPONSORING/MONITORING AGENCY REPORT NUMBER(S) AFRL-RB-WP-TR-2008-3170	
12. DISTRIBUTION/AVAILABILITY STATEMENT Approved for public release; distribution unlimited.					
13. SUPPLEMENTARY NOTES Report contains color. PAO case number AFMC-2008-0081; cleared 22 December 2008. See also Volume 2 (AFRL-RB-WP-TR-2008-3171).					
14. ABSTRACT This report will summarize the work performed to better understand the aerodynamics and potential benefits to using a biplane configuration with endplates in the aerodynamic regime experienced by a small unmanned aerial vehicle (UAV). Topics investigated include aerodynamic lift and drag, as well as a vehicle sizing study. Wind tunnel testing resulted in the conclusion that there is a substantial difference between positive and negative stagger; it also exposed a 'kink' in the lift curve of the biplane with endplates. Apparently this 'kink' has been in the literature for over 75 years, yet no direct reference to it or its source has been found. Results from 2-dimensional and 3-dimensional flow diagnostic techniques, as well as theoretical analyses are used to better understand these phenomena. Also provided is a mission-specific example of where the systems-level benefit (combined aerodynamic and structural/weight) of a biplane configuration with endplates exists after several iterations through a conceptual design and sizing process.					
15. SUBJECT TERMS Houck, biplane, end plates, flow guides, wing tips, gap, stagger, low Reynold's number					
16. SECURITY CLASSIFICATION OF:			17. LIMITATION OF ABSTRACT: SAR	18. NUMBER OF PAGES 82	19a. NAME OF RESPONSIBLE PERSON (Monitor) Cale H. Zeune 19b. TELEPHONE NUMBER (Include Area Code) (937) 255-0161
a. REPORT Unclassified	b. ABSTRACT Unclassified	c. THIS PAGE Unclassified			

Table of Contents

Section	Page
Table of Contents	iii
List of Figures	v
List of Tables	ix
Acknowledgements	x
Nomenclature	xi
1 Executive Summary	1
2 Introduction	3
3 Background	4
3.1 Review of the Literature	4
3.2 Theoretical Analysis	5
4 Lift: Vortex Lattice Results	8
4.1 Decalage Effect	8
4.2 Dihedral Effect	10
4.3 Sweep Angle Effect	11
4.4 Overhang Effect	12
4.5 The Effect of Stagger	13
4.6 The Effect of Gap	16
4.7 The Two Most Significant Parameters: Gap and Stagger	18
5 Lift: Experimental Results	19
5.1 Effect of Changes in Stagger	20
5.2 Effect of Changes in Gap	24
5.3 Downwash Relations	26
5.4 Kutta-Joukowski Integrated Circulation Derived Lift	29
5.4.1 K-J Lift: Stagger	29
5.4.2 K-J Lift: Gap	29
5.5 Generalized Equation for Biplane Lift	31
5.6 Change in Lift Curve Slope, or, “The Kink”	32
6 Drag: Experimental Results	36

6.1	Effect of Changes in Stagger.....	36
6.2	Effect of Changes in Gap	38
6.3	Comparing the Orthogonal Biplane and Equivalent Monoplane Models to the Force Balance Results	40
6.4	Momentum Deficit, Blasius Flat Plate, and Vortex Drag	42
6.5	Wake Vortex Morphology	43
7	Design.....	48
7.1	Background	48
7.2	Problem Statement	48
7.3	Requirements.....	48
7.3.1	Functional requirements.....	48
7.3.2	Requirements and design space.....	48
7.4	Structural Analysis	50
7.5	Comparison with the Biplane.....	53
7.6	Comparison to an Equivalent Monoplane	54
7.7	Aerodynamic analysis	58
8	Conclusions	61
8.1	Flow Physics	61
8.2	Design.....	62
9	References	64

List of Figures

Figure	Page
Figure 1 Biplane Parameters: Dècalage, Stagger, and Gap.	4
Figure 2 span efficiency for nonplanar systems ($\text{gap}/\text{span} = 0.2$).....	5
Figure 3 Gap/Span vs. Munk's Factor [14].....	6
Figure 4 shows little variation of the lift to drag ratio for varying dècalage angles.	9
Figure 5 comparison of the Decalage effect between the AVL and NACA results show good agreement up until stall inception in the experimental results.....	9
Figure 6 Lift Coefficients vs. Dihedral (at an angle of attack 5) show comparatively little variation across a wide range of values.....	10
Figure 7 comparison of Dihedral effect between AVL and NACA results shows good agreement.....	11
Figure 8 L/D vs. Sweep Angle for different staggers shows adverse effects on the lift to drag ratio as sweep angle increases.	11
Figure 9 CL vs. Overhang (at an angle of attack 5) shows adverse effects for the lift coefficient as overhang ratio increases or decreases.	12
Figure 10 Comparison of Overhang effect between AVL and NACA results shows good agreement.	13
Figure 11 a comparison of AVL results shows no visible differences between negative and positive stagger with 1.0C stagger, 0.5 gap and 1.0C stagger, 1.0C gap.....	14
Figure 12 the variation of Lift coefficient with varying stagger (at a 5 degree angle of attack), the greatest variation is seen within 1 chord length stagger with a sharp drop-off in variation beyond that.....	16
Figure 13 plot shows the variation of Lift coefficient with varying gap (at a 5 degree angle of attack), clearly the greatest variation occurs within one chord length gap for most staggers.....	17
Figure 14 comparison of gap and stagger effect between AVL and NACA results shows similar behavior for biplanes.....	18
Figure 15 shows a clear dependence of lift on stagger at constant gap.	21
Figure 16 shows dependence of lift on stagger at constant gap with decreasing effect at a higher gap.	21
Figure 17 combines the UD LSWT experimental results with the AVL results which compare well up to approximately 5 degrees where it is suspected viscous effects begin to dominate the flow even at $\text{Re } 120,000$. Model #3 (0.5C gap, (+) and (-) 0.5C stagger) and Model #4 (0.5C gap, (+) and (-) 1.0C stagger).....	22
Figure 18 uses streamwise PIV velocity contour data to elucidate the downwash behavior behind the biplane with endplates and consequently the lift behavior as a function of stagger (+1, 0, -1)	

and angle of attack. The numbers to the right of each contour figure represent measured downwash angles of the individual upper and lower wings.	23
Figure 19 shows representative results from the Trefftz plane PIV showing a portion of the spanwise distribution of downwash from the wingtip to 16% semi-span inboard becoming asymptotic.....	24
Figure 20 shows that at a negative stagger, lift is a strong function of gap even up to $2c$	24
Figure 21 shows there is still some dependence upon gap even at zero stagger.....	25
Figure 22 shows much less dependence on gap at a positive 1 chord stagger.....	25
Figure 23 streamwise PIV velocity contours behind two biplanes with different gaps ($0.5c$, $1.0c$) clearly show an increase in downwash angle behind the biplane with greater gap implying greater lift as well. The numbers to the right of each contour figure represent measured downwash angles of the individual upper and lower wings.	26
Figure 24 contrasts the downwash angles behind the upper and lower wings as a function of stagger at an angle of attack of 10 degrees with a superimposed integrated lift coefficient demonstrating the proportional relationship that still exists between lift coefficient and downwash.	27
Figure 25 Compares C_L determined through integrated force measurement to C_L calculated from ϵ for the upper and lower wings independently at a fixed gap of $0.5c$ and various staggers. All stagger cases compare quite well at lower α , but only the positive stagger case compares well at higher α	28
Figure 26 Tuft flow visualization of a 24" Houck Configuration at 50 mph ($Re\ 215,000$): progression of leading edge separation bubble for a positive stagger configuration (reproduced from Walker [2] with zero lift shifted angle of attack).....	28
Figure 27 shows that for the zero stagger and positive stagger cases, the K-J derived lift matches the integrated lift force derived results. For the negative stagger cases, the likely cause for the difference is a separation bubble as the suction lift would not be accounted for in Trefftz-plane integration of circulation.	30
Figure 28 shows that in the case of varying gap with zero stagger, K-J derived lift compares quite well with the integrated force derived lift without any hint of separation seen in the negative stagger cases. It is noted, however, that these lift curves are not well-matched by single linear curve fits.	31
Figure 29 compares the generalized empirical biplane lift equation to a configuration tested at AFIT using a gap and stagger not explicitly used in creating the empirical equation. The AFIT results have been zero lift shifted for the purposes of comparison since they used a NACA 2412 airfoil.....	32

Figure 30 shows how the lift curve appears to have a departure from a single linear curve fit.....	33
Figure 31 provides one example of the multiple linear curve fits possible when the region of transition is eliminated from the curve-fitting process. This behavior was seen uniformly across all models and Reynolds number tested.....	34
Figure 32 shows that the angle of stagger is the most relevant parameter in determining the magnitude of the change in lift curve slope from region I to region II.	34
Figure 33 highlights that the change in downwash slope mirrors the change in lift slope in and around the region of transition (or “kink”) as viewed from the perspective of the downwash angle of the upper and lower wings as determined through streamwise PIV.	35
Figure 34 shows that increasing stagger significantly decreases lift induced drag at higher coefficients of lift.....	36
Figure 35 shows how the shape and location of the spanwise velocity in the region of the wingtip changes as a function of stagger. These variations cause fundamental differences in the manner in which the wake rolls up thereby affecting the lift induced drag and the lift efficiency.	37
Figure 36 shows how the shape and location of the vertical velocity in the region of the wingtip changes as a function of stagger. Similar to the spanwise variations, these variations cause fundamental differences in the manner in which the wake rolls up thereby affecting the lift induced drag and the lift efficiency.	37
Figure 37 highlights the strong dependence of lift induced drag on gap at a stagger of (-) 1c.....	38
Figure 38 shows that with positive stagger [$s = (+) 1c$] the trend with increasing gap is not consistent in reducing lift induced drag.	38
Figure 39 shows that the vertical velocity contours have roughly the same shape in spite of a large difference in gap that corresponds to a large difference in overall lift performance. (zero stagger case).....	39
Figure 40 shows the spanwise velocity contours have a strong resemblance despite a large change in gap with a corresponding large difference in lift performance. (zero stagger case).....	40
Figure 41 provides an example where the orthogonal biplane model does a good job of predicting the measured drag.	41
Figure 42 is an example of where the equivalent monoplane model closely predicts the measured drag.	41
Figure 43 shows the orthogonal biplane prediction falling in between the positive and negative stagger measured drag.....	42

Figure 44 the different drag measurement methods compare extraordinarily well across a variety of staggers.	43
Figure 45 compares the radically different shape of the wake and the vertical velocity field around (a) curved (AFIT, Walker) and (b) flat plate endplates despite the fact that the two wings are loaded roughly the same. Angle of attack in (a) is 10 degrees and (b) 8 degrees.	44
Figure 46 compares the vastly different near and far wake vortex morphology at a roughly 5 degree angle of attack at (a) 22” downstream, (b) 42” downstream, and (c) 68” downstream.	45
Figure 47 compares the near and far wake vortex morphology in a more highly loaded case where the differences between cases is harder to discern. Roughly 12.5 degrees angle of attack, (a) 22” downstream, (b) 42” downstream, (c) 68” downstream.	45
Figure 48 shows that changing the upper/aft wing profile has a significant impact on the shape of the wake in both the near and far wake. ~ 5 degree angle of attack, (a) 42 inches downstream, (b) 68 inches downstream.	46
Figure 49 shows drastically different wake morphology between the lightly loaded (a) ~5 degree angle of attack and the more highly loaded case where the vortices merge (b) ~12.5 degree angle of attack and the upper/aft wing has been replaced by the NACA 0012.	47
Figure 50 Constraint Diagram defining the design space for a Small UAV with previous designs.	49
Figure 51 shows the structural models with their geometric characteristics.	50
Figure 52 is a screen snapshot of the stress distribution of model #1 with 1 gap and 0 stagger.	52
Figure 53 shows the variation in stress due to changes in stagger while keeping gap constant.	53
Figure 54 is a comparison of a traditional biplane with no endplates and two biplanes with endplates and different gaps.	53
Figure 55 shows the stress distribution of the equivalent monoplane.	55
Figure 56 shows the stress distribution of the equivalent monoplane with same span as the biplane (thus, lower effective aspect ratio).	57
Figure 57 is an example of the Equivalent Monoplane model created with AVL.	58
Figure 58 compares the lift curve generated using the UD-LSWT experimental data for the biplane configuration with endplates to the AVL results for the monoplane.	59
Figure 59 compares the aerodynamic efficiency of the biplane with endplates obtained from the UD- LSWT experimental data to the AVL results for the monoplane.	60

List of Tables

Table	Page
Table 1 <i>case numbers with stagger and gap with 0.25 chord length intervals</i>	15
Table 2 <i>Model Configurations</i>	20
Table 3 <i>lists the physical characteristics of the eight models</i>	51
Table 4 <i>calculated displacement and stress for each configuration</i>	51

Acknowledgements

This report is submitted in partial fulfillment of sub-recipient agreement # WBSC 9017UDA. Although the work is titled under the University of Dayton banner, it represents the work of a great many individuals. In particular, the following people have made a material contribution to the completion of the modeling, analysis, and/or the documentation of the effort:

Kang, Hantae – UD – Wind Tunnel Testing, PIV
Bichal, Abhishek – UD – Wind Tunnel Testing, PIV, PSV
Genco, Nicola – UD – Wind Tunnel Testing, Force
Landolfo, Giuseppe – UD – Conceptual Design and Sizing, Mission Definition, FEA
Altman, Aaron – UD – Wind Tunnel Testing, Program Management, Documentation
Altman, Servane – UDRI – Wind Tunnel Testing
Walker, Michael – AFIT – Wind Tunnel Testing, Force, Hot-Wire
Killian, Dermot – AFIT – Wind Tunnel Testing, Force
Reeder, Mark – AFIT – SLA, Wind Tunnel Testing & Prototyping
Barlow, Jewel – University of Maryland – Wind Tunnel Testing
Crafton, Jim – ISSI – PIV, Stereo PIV
Estevadeordal, Jordi – ISSI, Stereo PIV, Loaning his Nd:YAG
Bryant, Elaine – AFRL – Program Manager
Fry, Tim – UDRI – CFD, DOE, Program Management
Fry, Tracy – UDRI – DOE, Documentation
Houck, Ron – IHE – Concept Inventor, Prototype Build
Gillum, Christoph – SES, Inc – Wind Tunnel Model CAD
Maresca, Rich – WBI – Contract and Program Management
Groeber, Claudette – UDRI – Contract Management
Neely, Mike – UDRI – CAD and CFD Modeling
Staiger, John – AFRL - CFD
Tyler, Charlie – AFRL – CFD
Zeune, Cale – AFRL – Program Management

Nomenclature

AR	aspect ratio
b	span
b_U	upper wing span
b_L	lower wing span
c	chord
C_D	total drag coefficient
C_{Di}	induced drag coefficient
C_{DiEM}	Munk's induced drag coefficient
C_{DiOB}	Prandtl's induced drag coefficient
C_L	lift coefficient
C_{L_L}	lower wing lift coefficient
$C_{L_{max}}$	maximum lift coefficient
C_{L_U}	upper wing lift coefficient
C_{L_α}	lift curve slope
e	span efficiency factor
EM	Equivalent Monoplane
g	gap
I	electrical current
k	equivalent monoplane span factor
L/D	lift to drag ratio
n	load factor
OB	Orthogonal Biplane
Oh	Overhang Ratio (b_U / b_L)
P	power
R	A Distance Used in Calculating Downwash
Re	Reynolds Number
s	stagger
S	Reference Planform Area
T	thrust
v	induced velocity
\bar{V}	induced velocity for a vortex segment

V	flow speed
V_{stall}	stall velocity
W	takeoff weight
α	angle of attack
δ	coefficient of mutual influence
ε	downwash angle
ρ	density
ρ_{SL}	sea level air density
σ	angle of stagger
σ	stress

1 Executive Summary

This report will summarize the work performed by the University of Dayton subsequent to Phase I to better understand the aerodynamics and potential benefits to using a biplane configuration with endplates in the aerodynamic regime experienced by a small UAV. The documentation will be subdivided into the following sections:

1. Aerodynamic Lift
2. Aerodynamic Drag
3. Mission Definition and Monoplane vs. Biplane Air Vehicle Conceptual Design Study with Integrated Aerodynamic and Structural Analysis used to identify the Configuration Best Suited to Perform the Defined Mission.

Sections 1 and 2 will present numerous significant results. The integrated force study resulted in the conclusion that there is a substantial difference between positive and negative stagger. This result is a direct contradiction to the predicted results of Munk. The integrated force study also exposed a “kink” in the lift curve of the biplane with endplates. Apparently this “kink” has been in the literature for over 75 years, yet no direct reference to it or its source has been found.

Results from 2-dimensional and 3-dimensional flow diagnostic techniques will then be used to better explain the differences uncovered in the force study in positive and negative stagger, as well as the “kink” in the lift curve. It is most a viscous effect since the potential flow results do not show similar behavior; however, there is very little dependence of the behavior of the “kink” on Reynolds number in the range tested (60,000 to 120,000). Since the lift curve is linear with one slope before the kink, and again linear with a different slope after the kink, suction lift is not suspected. In addition, 2-dimensional streamwise momentum deficit drag accounts for the vast majority of the 3-dimensional drag measured by the force balance indicating the unlikelihood of significant rotational effects. It is thus noted that the source of the “kink” in the lift curve is still not fully understood, though it appears to always occur around the point of maximum lift to drag ratio. Therefore it is believed that whatever is at the source of the kink increases drag faster than it increases lift. Many successful connections are made, nevertheless, between the integrated force results and the flowfield results (using Kutta-Joukowski Integration of Lift, Momentum Deficit Drag, Downwash angle related to lift), and some related back to Munk’s equivalent monoplane and Prandtl’s orthogonal biplane theorems.

Section 3 will provide a mission-specific example of where the systems-level benefit (combined aerodynamic and structural/weight) of a biplane configuration with endplates exists after several iterations through a conceptual design and sizing process.

Sections 1 and 2 will introduce only the existing relevant literature to provide a context for the technical contributions contained within this report. These sections will leverage work already performed on this project at the Air Force Institute of Technology, the U.S. Air Force Academy, and the University of Maryland in order to generalize the conclusions made from the results obtained at the University of Dayton. One resulting example is a generalized empirical equation to predict the lift curve as a function of gap, stagger and aspect ratio that accurately captures the large differences between positive and negative stagger observed not reflected in Munk's theorem.

2 Introduction

Suitable background on the Houck project has already been provided in numerous previous reports through UDRI. Thus, this report will not repeat the background and motivation for the project as a whole. For those details, the reader is referred to Volume II [¹]. In addition, no effort will be made in this report to duplicate the previous documentation of work performed for this project by AFIT [²] [³], the US Air Force Academy [⁴], AFRL, The University of Maryland [⁵], the University of Dayton Doctoral dissertation by Kang [⁶], or the University of Dayton Master's theses of Genco [⁷] or Landolfo [⁸]. If the reader is interested in these detailed results, they are referred to the respective reports, papers, theses and dissertation. The focus of this report is to provide a comprehensive summary of all work performed on the Houck project in the context of the findings of the flow physics and design efforts performed by the Department of Mechanical and Aerospace Engineering at the University of Dayton.

The process of aerodynamic development and realization of a new aircraft configuration requires a fundamental preliminary investigation into the most influential factors, and how these factors modify the performance and behavior of the configuration. The next logical step is to determine the optimal performance of the configuration as a whole based on prediction of how these individual factors affect the aerodynamic efficiency. One objective of this report is to present this fundamental parametric study on a biplane joined at the tips by endplates.

Because few studies into the actual physics of flow interaction between multiple planar lifting surfaces have been conducted, the parameter space is quite rich. It is important, as a first step, to understand which factors influence the performance of a biplane and furthermore, a biplane joined at the tips by endplates. This investigation begins with a parameter study performed using a vortex lattice code to reduce the experimental parameter space. Once the experimental parameter space is reduced, wind tunnel models are selected based on variation of the relevant parameters. Force balance data are used in unison with off-body Digital Particle Image Velocimetry results in 2 and 3 dimensions to explain the most relevant observations. Discussion of these aerodynamic results is subdivided into Biplane lift and then Biplane drag. A candidate small UAV mission is then described and an investigation will be detailed that uses the aerodynamic results obtained for this report in tandem with finite element structural analysis substituted into a conceptual aircraft design and sizing methodology.

3 Background

Discussion begins with a basic review of existing Biplane nomenclature and literature. Figure 1 shows the section of a two-dimensional biplane by a plane perpendicular to the span, giving two profiles, whose chords are inclined at the angle δ called the d  calage, which is assumed positive when the upper wing is at greater incidence than the lower, as in the diagram.

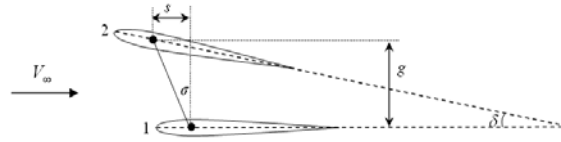


Figure 1 Biplane Parameters: D  calage, Stagger, and Gap.

The gap g is defined as the vertical distance between the leading edges of the two wings perpendicular to the free stream, and stagger s is the distance between the two wing leading edges parallel to the freestream. The stagger can also be defined by the angle σ between the vertical line and the line joining the quarter chord of the wings, and it is equal to:

$$\sigma = \tan^{-1} \frac{s}{g}$$

There is no defined convention for positive stagger. In this report, the stagger is assumed positive when the upper wing is fore of the lower wing. Both gap and stagger are referenced to the chord length of the model.

Now that the basic nomenclature has been presented, a brief review of the literature will be included. Much relevant work has been done on the problem of multiple lifting surfaces, though none of these biplanes were joined at the tips with endplates and few investigations focused on the physics of the flow interactions between wings.

3.1 Review of the Literature

The first important contribution this paper takes into account is the theory of Betz [⁹][¹⁰] in 1914, elaborated then by Fuchs [¹¹] and given in its final form by Fuchs and Hopf [¹²] in 1934. This theory explained the first computation of the mutual interference effect of 2 airfoils which led to practical formulas. This theoretical development was based on steady, incompressible, inviscid and irrotational fluid mechanics. These results were then discussed by Diehl [¹³] in 1934 in a report that combined

experimental and theoretical data to derive a series of curves from which the lift curves of the individual wings of a biplane might be obtained.

From a theoretical point of view, the most fundamental papers were the contributions of Prandtl and Munk [14] who determined the lift distribution providing the minimum induced drag of a biplane, and whose work also contain general theorems on the induced drag of biplane lifting systems.

In applying vortex techniques to non-planar wings, Kroo [15] describes that drag due to wingtip vortices contribute to 40% of the total drag in monoplanes. A nonplanar wing design can potentially reduce the effect these wingtip vortices have on the aerodynamic efficiency of the configuration. His wing configurations and their associated efficiencies are shown in Figure 2.

In another more recent study, Ahmed and Archer [16] described a study of biplane efficiency with endplates where the chord length of the endplate relative to the wing chord length was varied. They determined that an endplate with 30% of the chord of the wing was essentially equally as effective in terms of aerodynamic efficiency as endplates with greater area.

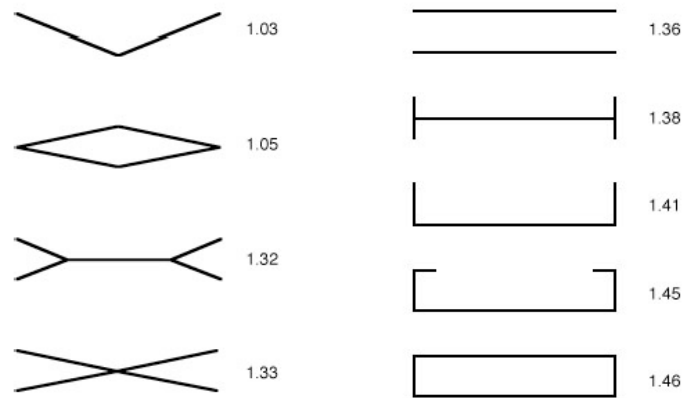


Figure 2 span efficiency for nonplanar systems (gap/span = 0.2).

3.2 Theoretical Analysis

The early development of biplane and equivalent monoplane theory will be briefly presented since it will later be used in comparison to the results obtained during the Houck configuration studies.

Munk [17] explained the performance of a biplane with varying stagger analytically and also considered the effects of varying chord length and d  calage. He compares the induced drag between a monoplane and a system of wings and concludes that under similar conditions a single airfoil with a span k times the maximum span of a system of airfoils has the same induced minimum resistance as the combined system. Where, k is a factor characteristic of the system of airfoils. Munk [14] also derived comparatively simple formulas to calculate ΔC_L for biplanes with staggered configurations or d  calage.

In General Biplane Theory Munk derived some useful formulas using theoretical and experimental data. He found the additional lift coefficient of staggered wings to be:

$$\Delta C_L = \pm 2C_L \frac{S}{b^2} \left(\frac{1}{k^2} - 0.5 \right) \frac{b}{R} \frac{st}{b}$$

Where, S is the total area, st the stagger, b the span, k the equivalent monoplane span factor, and R a distance used in calculating the induced downwash. $\left(\frac{1}{k^2} - 0.5 \right) \frac{b}{R}$ is a function of the ratio of gap to span, g/b , which is called the ‘Munk factor’. Figure 3 shows that when the gap increases (holding span constant), Munk’s factor decreases and, consequently, C_L decreases.

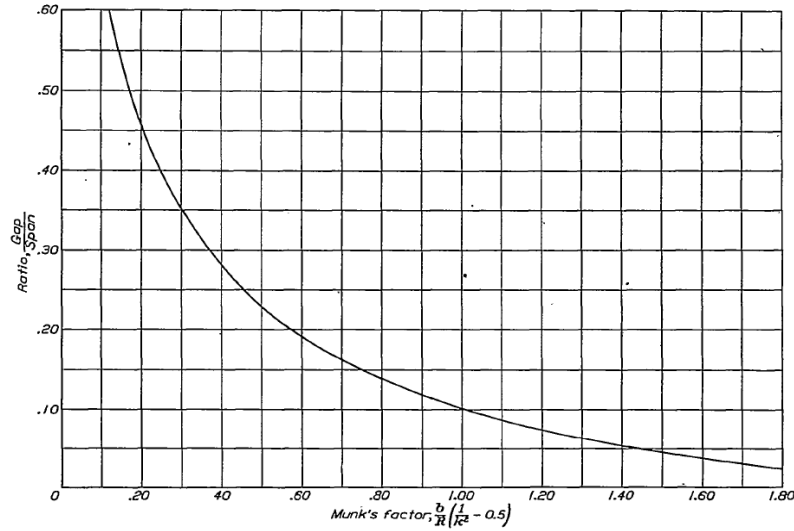


Figure 3 Gap/Span vs. Munk’s Factor [14].

Induced drag calculations are performed by applying the formula developed by Munk [17] which states that:

$$C_{D_{iEM}} = \frac{C_L^2}{\pi} \frac{S}{b^2 k^2}$$

where S is the entire area, b is the span, and k denotes the equivalent monoplane span factor which depends merely on the gap/span ratio of the biplane. If the two spans of a biplane are slightly different, an average span is to be substituted. The values of k are determined by Munk [14]. For a rough estimate it is even sufficient to take $k = 1$ for all monoplanes and $k = 1.1$ for all biplanes. This approach to the induced drag calculation is also called “equivalent monoplane”.

From these results, it appears that gap and stagger have a strong influence in obtaining additional lift force in biplanes. Another approach, called “orthogonal biplane” was developed by Prandtl [18], and it states that the induced drag coefficient is equal to:

$$C_{D_{iOB}} = \frac{C_L^2}{\pi} \frac{S}{b^2} (1 + \delta)$$

where δ is the coefficient of mutual influence which depends upon gap/span ratio, and it is equal to:

$$\delta \cong \frac{1 - 0.66 g/b}{1.05 + 3.7 g/b}$$

Neither Prandtl's or Munk's theories take into account the effect of stagger because, as stated in Munk's Stagger Theorem: *“The total induced drag of any multiplane lifting system is unaltered if any of the lifting elements are moved in the direction of the motion provided that the attitude of the elements is adjusted to maintain the same lift distribution of lift among them.”*

Diehl [17] specified the lift coefficients of the individual wings of a biplane as given by $C_{L_U} = C_L + \Delta C_{L_U}$ and $C_{L_L} = C_L - \Delta C_{L_L}$. Here, ΔC_{L_U} is a function of gap, stagger, aspect ratio, dècalage, overhang ratio and wing thickness.

The aforementioned results comprise most of what is generally accepted today to be an accurate representation of biplane characteristics. It will be shown, however, that at least in the flow regime tested in this report, the results generated in the early third of the 20th century are only valid for a very limited range of angles of attack.

4 Lift: Vortex Lattice Results

Computational analysis was carried out to determine the geometric variables most affecting the aerodynamic performance of biplane configurations using AVL, developed by Youngren and Drela of MIT. The code utilizes a vortex-lattice representation of the lifting surfaces, and it assumes steady, irrotational, inviscid, incompressible attached flow. A number of test cases were also run for validation using Kroo's LinAir Pro and a NASA code modified by Mason called VLMpc and the results were found to agree to within better than 95%.

AVL was first used to eliminate possible influential parameters thought less likely to have an effect on aerodynamic performance such as dècalage, dihedral/anhedral, sweep, and overhang ratio. These results will be briefly presented first and compared to results in the literature where available for validation of the methods used.

Generalized dimensions were used for the computational analysis of the box-wing configurations. The absolute dimensions used for experimentation are a wingspan of 24 inches for each wing with a total wing area of 192 in² for both wings combined. This gave an AR= 6 [monoplane] for each wing. The AVL test conditions also included the density of air at sea level.

4.1 Decalage Effect

Dècalage on a biplane is defined as the acute angle between the mean chord lines of the two lifting surfaces. Five different dècalage angles varying from -4 to +4 with a 2-degree interval are considered. Figure 4 shows the results for lift to drag ratio using AVL. Results show little variation in overall aerodynamic performance as a result of dècalage.

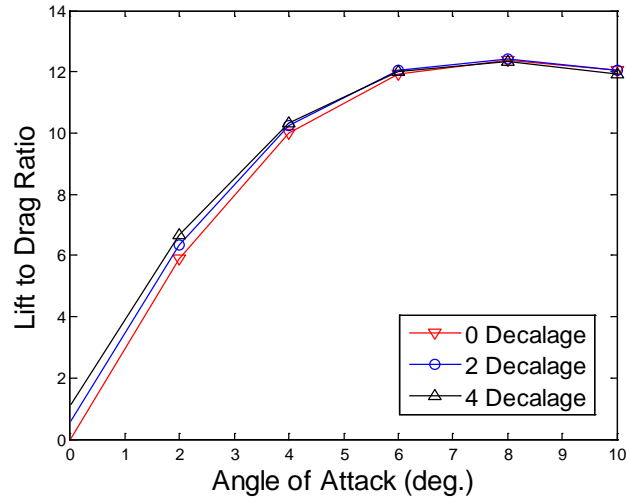


Figure 4 shows little variation of the lift to drag ratio for varying d calage angles.

These results were corroborated using the wind tunnel test results from a NACA Technical Report by Knight and Noyes [19] where good agreement was found at lower angles of attack. At higher angles of attack, results from AVL deviate from the wind tunnel tests (Figure 5).

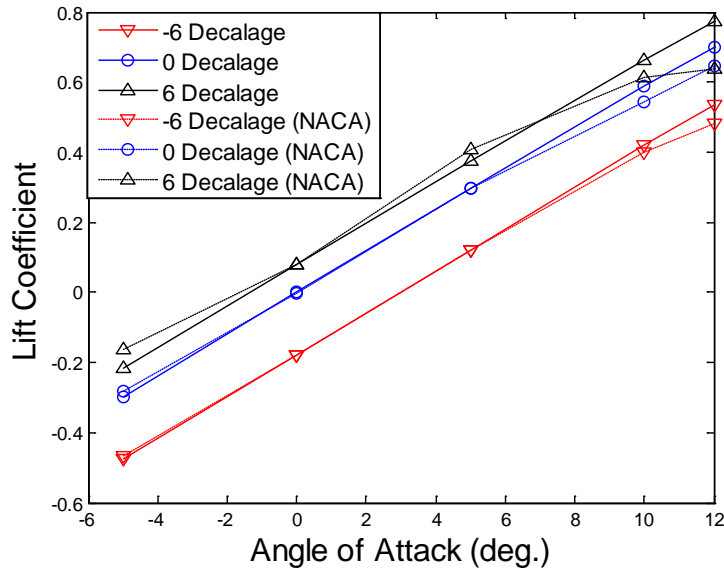


Figure 5 comparison of the Decalage effect between the AVL and NACA results show good agreement up until stall inception in the experimental results.

Results from AVL show a constant lift curve slope, whereas the slope of the lift curve from wind tunnel tests decreases as expected as the stall angle is approached when viscosity is present. According to Munk [14] the effect in C_L is observed as a result of a shift in the lift curve with increase in d  calage.

4.2 Dihedral Effect

The effect of dihedral on the lift curve is plotted in Figure 6. Three of the four configurations tested resulted in either no advantage or a disadvantage in the generation of lift from the wing configuration. A positive effect and the highest lift coefficient were obtained for the biplane configuration with dihedral on the upper wing and anhedral on the lower wing. The total change in lift coefficient found in variation of dihedral/anhedral was less than 6% and is insignificant compared to the changes due to other parameters evaluated.

A comparison of the wind tunnel tests of Knight and Noyes to the results from AVL is shown in Figure 7. Throughout the linear range for lift, the results are in good agreement. Disagreement is observed when the assumptions behind the vortex method fail to consider the viscous effects in the flow, near the onset of stall.

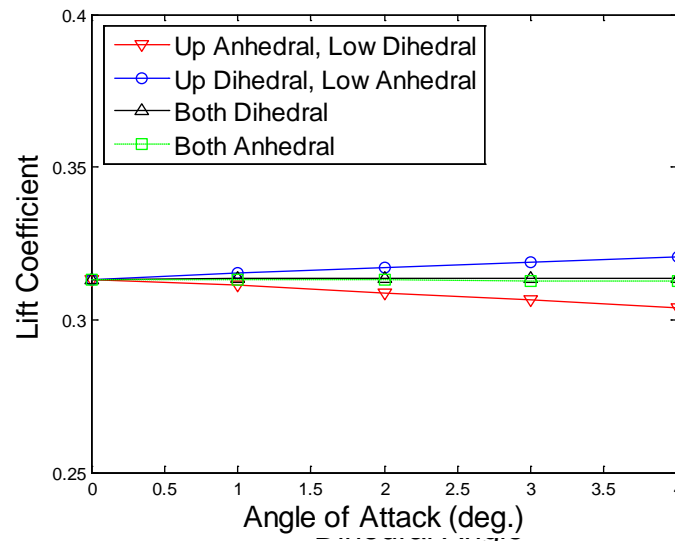


Figure 6 Lift Coefficients vs. Dihedral (at an angle of attack 5) show comparatively little variation across a wide range of values.

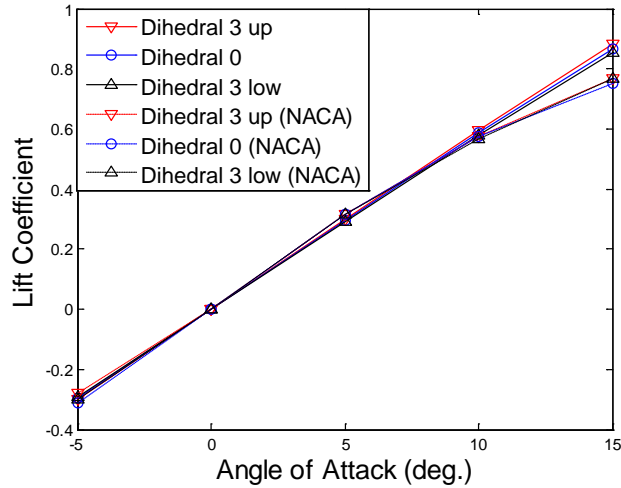


Figure 7 comparison of Dihedral effect between AVL and NACA results shows good agreement.

4.3 Sweep Angle Effect

Figure 8 shows L/D vs. angle of attack curves with varying sweep angles. Adverse effects on the performance of the biplane wing configuration with increasing sweep angle are observed. These adverse effects increase nonlinearly as sweep angle is increased. Although the changes between 30 and 60 degrees sweep angle are significant, they do not deviate from expected monoplane swept wing behavior. Thus, sweep angle will not be a parameter of interest in the experimental study.

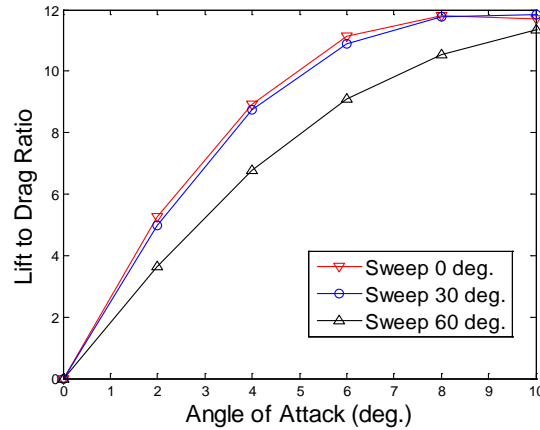


Figure 8 L/D vs. Sweep Angle for different staggers shows adverse effects on the lift to drag ratio as sweep angle increases.

4.4 Overhang Effect

The overhang ratio for a biplane is defined here as the ratio of the span of the upper wing to the span of the lower wing. Figure 9 shows CL as a function of overhang ratio from AVL with varying overhang ratios. Lift coefficient results show a bell curve where the maximum CL is obtained at an overhang ratio equal to 1.

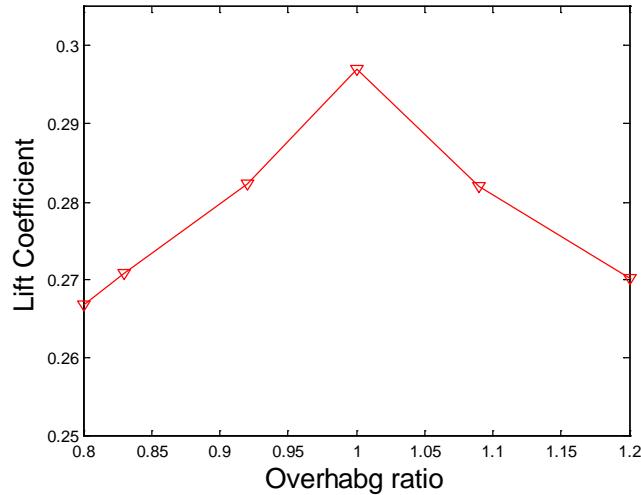


Figure 9 CL vs. Overhang (at an angle of attack 5) shows adverse effects for the lift coefficient as overhang ratio increases or decreases.

An increase or decrease in overhang ratio causes a decrease in L/D as displayed in the figure. A change in overhang ratio causes the endplates to close in on one of the main wing surfaces, which in turn causes the overall effective gap to be reduced. This effective decrease in the gap causes the lift of the wing combination to be reduced. As mentioned, Prandtl theoretically described the box shaped wing configuration as the best configuration where the overhang ratio of the wing is 1 [18]. Kroo also shows that the highest aerodynamic efficiency is obtained from the box shaped wing [15].

Figure 10 shows a comparison of the data from AVL to the wind tunnel data generated by Knight et al [19]. Their wind tunnel results show good agreement when superimposed over the AVL results. The slight variation can be attributed to the presence of viscosity in the NACA wind tunnel results.

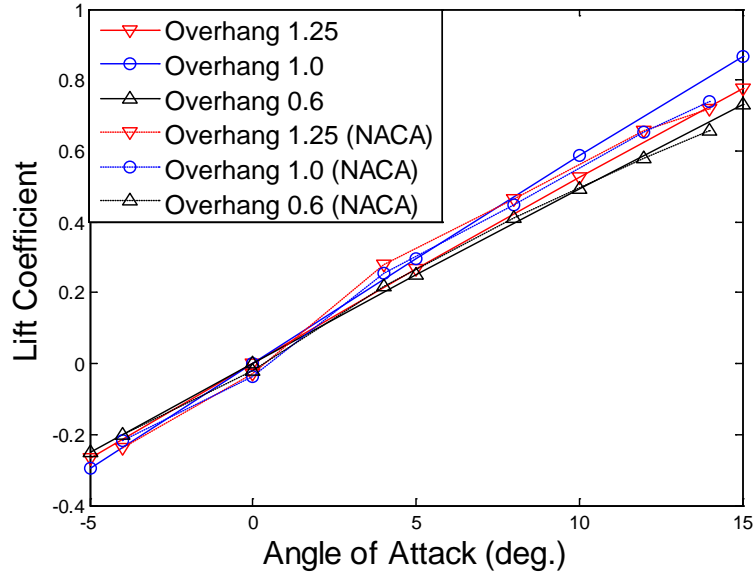


Figure 10 Comparison of Overhang effect between AVL and NACA results shows good agreement.

4.5 The Effect of Stagger

Figure 11 is a comparison between the negative and positive stagger configuration of two models using AVL. Lift coefficients at positive and negative stagger can be seen to have very similar values. The difference was just 0.01%. Although this is a non-physical result, it leads to the belief based on the AVL results and Munk's theoretical results that negative and positive stagger configurations with the same gap have the same aerodynamic characteristics. AVL has some limitations in discerning the measured differences in positive and negative stagger that will be highlighted using the UD experimental results later.

For the parametric study across the variables, 90 cases are selected based on a gap and stagger increment of 0.25 chord lengths as displayed in Table 1. Based on the AVL results of the negative and positive stagger configuration, these two stagger configurations were considered the same configuration in this AVL analysis (steady, inviscid, irrotational, incompressible).

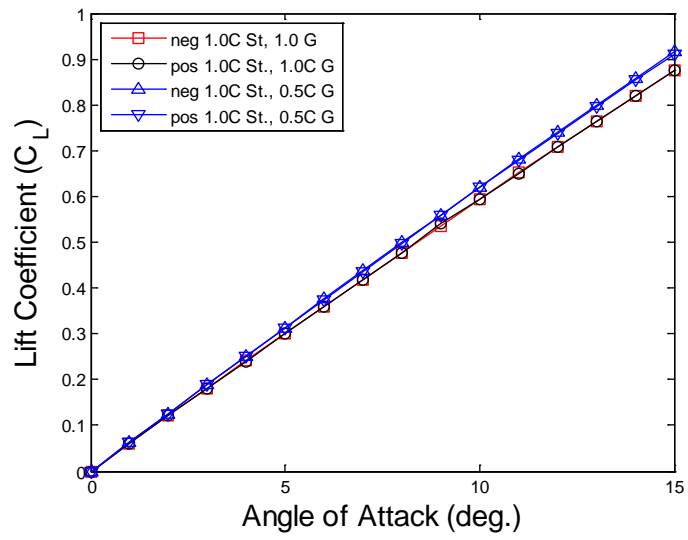


Figure 11 a comparison of AVL results shows no visible differences between negative and positive stagger with 1.0C stagger, 0.5 gap and 1.0C stagger, 1.0C gap.

Table 1 case numbers with stagger and gap with 0.25 chord length intervals.

		Gap								
		C	.25C	.5C	.75C	C	.25C	.5C	.75C	C
Stagger (Positive or Negative)	C									
	.02C	0	1	2	3	4	5	6	7	8
	.25C	9	0	1	2	3	4	5	6	7
	.5C	8	9	0	1	2	3	4	5	6
	.75C	7	8	9	0	1	2	3	4	5
	C	6	7	8	9	0	1	2	3	4
	.25C	5	6	7	8	9	0	1	2	3
	.5C	4	5	6	7	8	9	0	1	2
	.75C	3	4	5	6	7	8	9	0	1
	.0C	2	3	4	5	6	7	8	9	0

C : chord length

To study the effect of stagger, values of stagger between 0 and 2 chord lengths at increments of 0.25C are considered. The results in Figure 12 are plotted at values of constant gap for an angle of attack at 5 degrees. This graph shows the variation in lift coefficient with varying stagger at a 5 degree angle of attack. This angle of attack was chosen as representative of all below stall angles of attack. In addition, 5 degrees angle of attack was selected since it is near the maximum lift to drag ratio angle of attack where lift induced and parasite drag should be equal. The x-axis in the figure represents varying stagger from 0 to 2 chord lengths. The bottom solid line with triangular symbols is the smallest gap and it shows the

largest functional dependence. The highest line is the largest gap and it shows the smallest functional dependence across the range of stagger values investigated. Also, it is clear that large variations continue up to 1 C, and very small changes occur beyond 1 C.

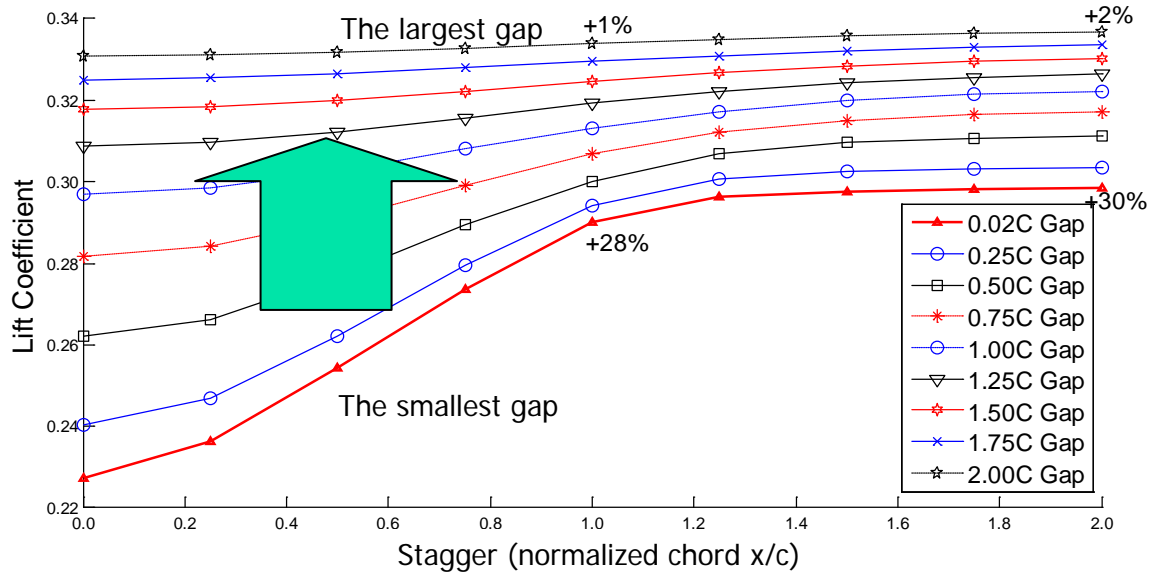


Figure 12 the variation of Lift coefficient with varying stagger (at a 5 degree angle of attack), the greatest variation is seen within 1 chord length stagger with a sharp drop-off in variation beyond that.

Munk [15] stated that the change in lift due to stagger is proportional to the square of the stagger distance, and he stated this relation is exact enough up to $1/3C$ stagger. For greater values of stagger equal to multiples of the chord, the dependence of lift on stagger is quite different. At these values of stagger, however, some would consider these to be no longer biplane configurations but more like tandem wing configurations. The change in lift of the upper and the lower wing is directly proportional to stagger, as long as the stagger is small.

4.6 The Effect of Gap

The results of the computational study of the effect of gap on the lift generated are plotted in Figure 13. It is observed that the lift coefficient, at 5 degrees angle of attack, is a stronger function of the gap between the two wings of a biplane. Increasing the gap between the two lifting surfaces of a biplane will result in an increase in the total lift coefficient. A greater rate of increase in lift coefficient as a function of increasing gap is observed until the gap reaches approximately 1 chord length distance. Above one chord length gap, the rate of change of lift coefficient decreases with increasing gap. Further

increases in the gap result in minimal interaction between the wings and leads to the lifting surfaces acting individually. Thus, from an air vehicle design perspective, any gap greater than a 1 chord length distance between the individual wings of the box-wing configuration would likely not merit consideration unless there were other design constraints that drove the gap to a larger value. A more detailed coupled structural-aerodynamic design study supporting this argument will be presented later in this report.

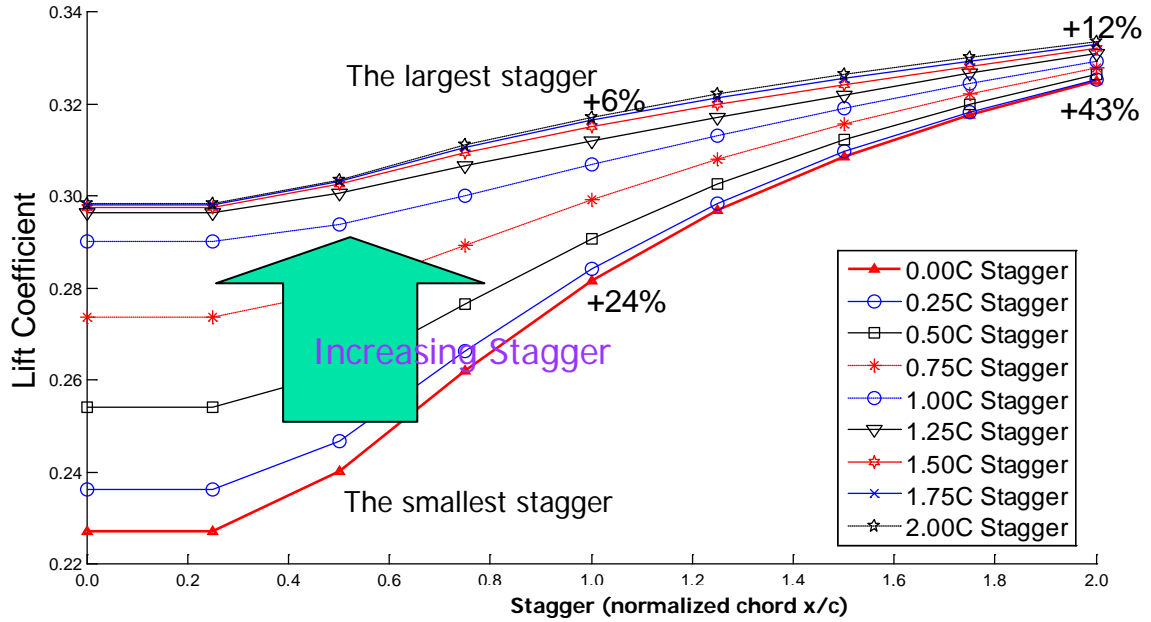


Figure 13 plot shows the variation of Lift coefficient with varying gap (at a 5 degree angle of attack), clearly the greatest variation occurs within one chord length gap for most staggers.

A similar result is also shown in Knight and Noyes [16]. Figure 14 shows a comparison of the data from AVL to the wind tunnel data by Knight et al in their report. A gap of 0.75C and three varying staggers ((-) 0.25C, no stagger, (+) 0.50C) were considered. The results from the NACA wind tunnel show good agreement with the results from AVL for the (+) 0.50C and no stagger configurations. The negative stagger configuration, however, has a different result: the C_L of this configuration is the lowest from the NACA report. As mentioned, AVL has a restriction in generating stagger. Therefore, the inviscid assumption of AVL is likely responsible for the difference between the two stagger configurations.

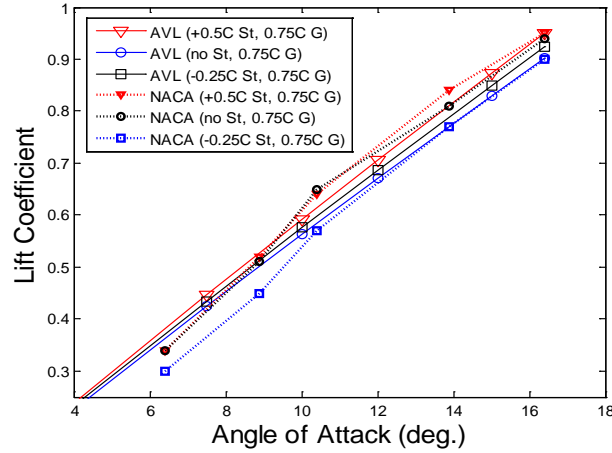


Figure 14 comparison of gap and stagger effect between AVL and NACA results shows similar behavior for biplanes.

4.7 The Two Most Significant Parameters: Gap and Stagger

The AVL results show that the parameters gap and stagger have the most major effects out of the six parameters studied for the biplane with endplates when aspect ratio and the total wing area are held constant. Other parameters considered for their influence on the aerodynamic performance of the biplane configuration include dihedral, dècalage, sweep and overhang. The effect of these parameters was observed to be either negative or negligible. Dècalage and dihedral under certain conditions could have a positive effect on the performance of the box wing configuration; however, these effects are comparatively small and were neglected for the purposes of this study. Variation of overhang and sweep had a negative effect on the performance at the Reynolds numbers tested. An increase or decrease in overhang caused the effective gap between the two wings to decrease. This resulted in a negative effect on the lift coefficient. Many cases were successfully validated against existing data in the literature where available. From the biplane configuration parametric study obtained using AVL, the most relevant parameters for wind tunnel testing were unmistakably reduced to gap and stagger.

5 Lift: Experimental Results

In the interest of brevity, few details of the experimental procedure and set-up will be provided in this report. These details are exhaustively provided in references [6] and [7] and were considered ancillary to the conclusions made from the results presented in this report.

The wings used in the UD experimental wind tunnel tests are based on a flat plate airfoil section of thickness 1.27 mm. A semi-span wing in a vertical position was used to match the size and Reynolds number with a full-sized UAV. Asymmetric flow is prevented by mounting the model on the floor. Such an arrangement, though obviously unsuited for yaw tests, yields accurate pitch, lift, and downwash data at the maximum Reynolds number [20]. The gap between the half wing and the ground was measured to be 1.13 mm and it was filled with petroleum jelly to prevent interaction between the flow and the model resulting from any gap between the two.

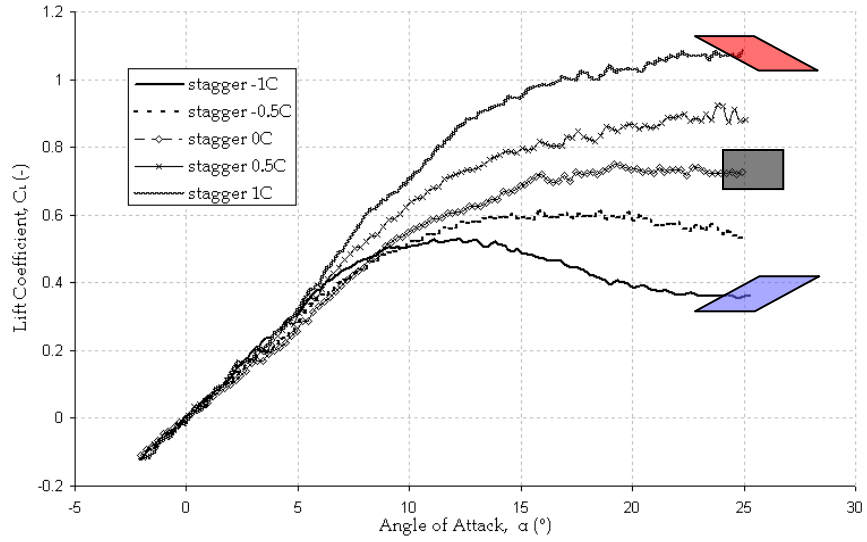
The fourteen different models selected for wind tunnel testing consisted of two identical wings, each having a chord length of 4 in. and a semi-span of 12 in., yielding a semi-span aspect ratio per wing of three, and are represented in Table 2 where c represents the chord length and the angle σ was defined in Figure 1. Hysteresis in lift was expected and as such tested for at both Reynolds numbers. No significant hysteresis was found. For a more detailed analysis, the reader is referred to [6] and [7]. In addition, there was less than a 2% difference between parametric results at different Reynolds numbers. This result was unexpected in the context of results to be explained later in this report however the implications are that viscous effects on the results are minimal in the range of Reynolds number tested.

Table 2 Model Configurations.

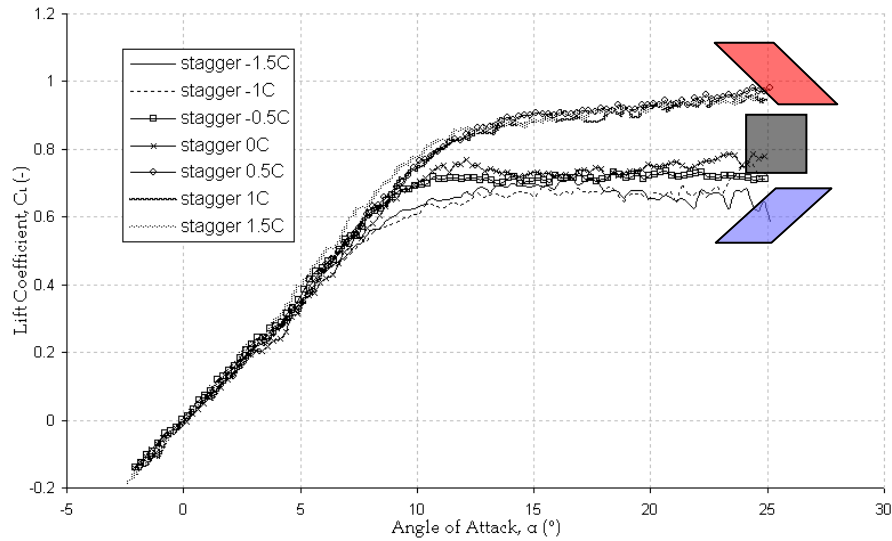
MODEL #	GAP	STAGGER	σ
1	1c	0c	0
2	0.5c	0c	0
3	0.5c	-0.5c	-45°
4	0.5c	-1c	-63.4°
5	1c	-0.5c	-26.6°
6	1c	-1c	-45°
7	2c	-1c	-26.6°
8	1c	-1.5c	-56.3°
9	0.5c	0.5c	45°
10	0.5c	1c	63.4°
11	1c	0.5c	26.6°
12	1c	1c	45°
13	2c	1c	26.6°
14	1c	1.5c	56.3°

5.1 Effect of Changes in Stagger

The purpose of this analysis was to experimentally study the effect of changes in stagger at constant gap. The results are presented for models with the same gap at each Reynolds number. Figure 15 and Figure 16 show the lift curve, C_L , vs. α for the $g = 0.5c$ and $g = 1c$ gap configurations respectively both at a Reynolds number of 60,000. Nearly identical curves were obtained at Reynolds number 120,000 so they were not included here. It is evident from the force data that increasing stagger increases lift performance beyond about 5 degrees angle of attack (roughly at maximum L/D). This is in sharp contrast to the AVL results and Munk's theoretical result which state the direction of stagger is irrelevant.



**Figure 15 shows a clear dependence of lift on stagger at constant gap.
 $g = 0.5c$, $Re = 60,000$.**



**Figure 16 shows dependence of lift on stagger at constant gap with decreasing effect at a
higher gap.
 $g = 1c$, $Re = 60,000$.**

Figure 17 contrasts the inviscid results from AVL with the UD-LSWT results. The two agree quite well up until approximately 5 degrees where it is suspected viscous effects begin to dominate. The higher Reynolds number case was used to demonstrate that large differences between positive and negative stagger were equally as substantial at the higher Reynolds number tested.

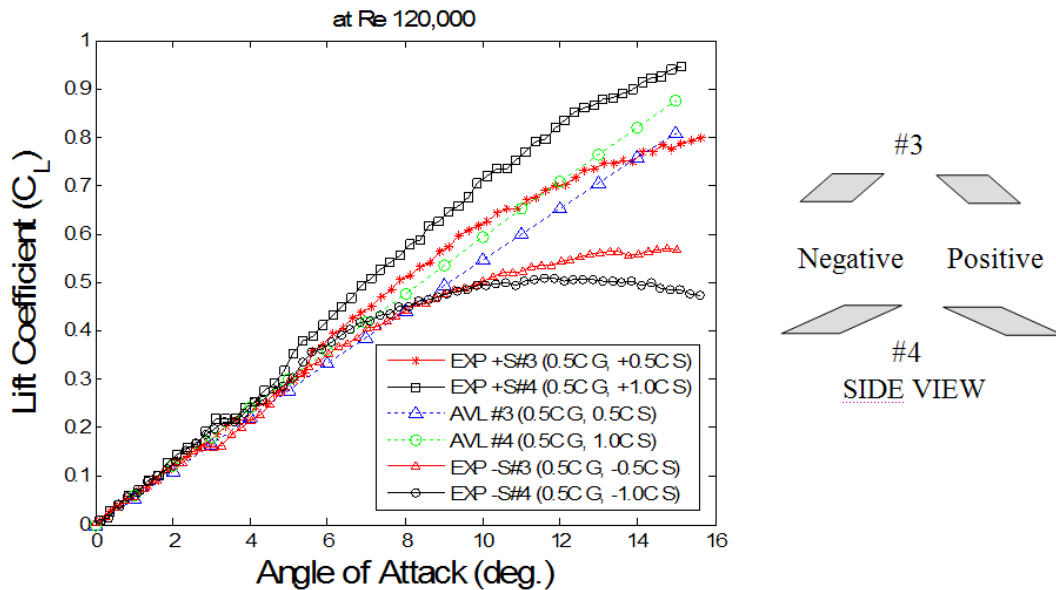


Figure 17 combines the UD LSWT experimental results with the AVL results which compare well up to approximately 5 degrees where it is suspected viscous effects begin to dominate the flow even at Re 120,000. Model #3 (0.5C gap, (+) and (-) 0.5C stagger) and Model #4 (0.5C gap, (+) and (-) 1.0C stagger).

Figure 18 allows some physical arguments to be made as to why this happens. There are tremendous differences in the downwash angles as a function of the degree of stagger of the configuration. As can be plainly seen for the positive stagger case at a 10 degree angle of attack, the downwash of the upper wing is considerably greater than that of the negative stagger case. This downwash will act to keep the airflow over the upper surface of the lower wing attached much longer and changes the effective angle of attack. This is also easily seen in the difference between the downwash angles of the lower wing from the positive to the negative stagger case at 10 degrees angle of attack. When comparing the difference in shear layer thickness between the upper and lower wing in a given image it is important to remember that for the positive and negative stagger cases, part of the shear layer in the image is temporally older by 1 chord length downstream (the stagger distance). Since the shear layer diffuses with distance downstream, this effect will give the illusion of a thicker shear layer on either the upper or lower wing surface depending on which one is further forward.

It is also expected that there would be some form of “jet” effect due to the virtual reduction/restriction in area between the two biplane wings when the downwash angles differ greatly in

instances such as higher angle of attack with positive stagger. This was not the case as seen in the figure; there is no discernible change in velocity in between the two wings relative to the freestream.

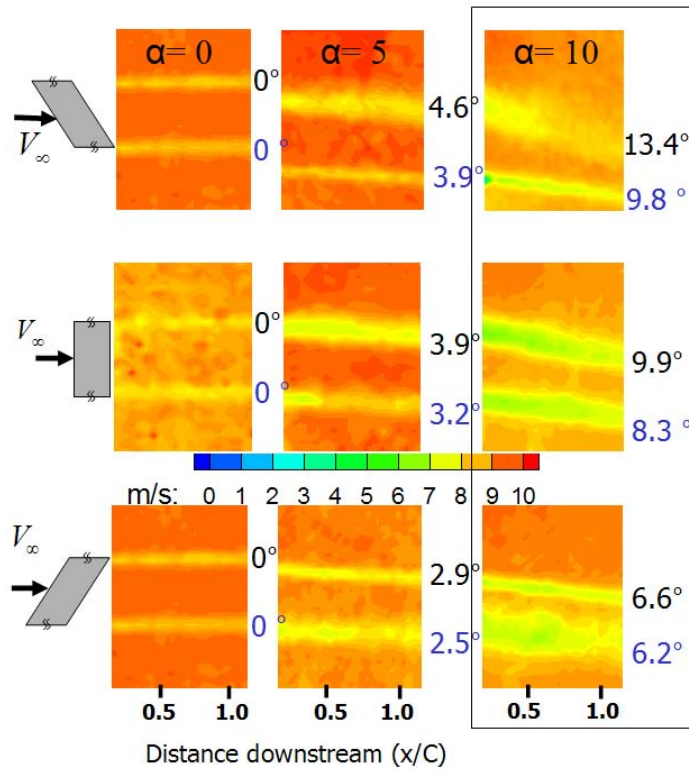


Figure 18 uses streamwise PIV velocity contour data to elucidate the downwash behavior behind the biplane with endplates and consequently the lift behavior as a function of stagger (+1, 0, -1) and angle of attack. The numbers to the right of each contour figure represent measured downwash angles of the individual upper and lower wings.

Although the PIV data shown represent only a single chordwise planar slice, Figure 19 shows that the data taken at a spanwise location of 33% semi-span inboard from the tip should be representative of most of the span since the downwash distribution appears to asymptote by approximately 16% of the semi-span inboard from the tip.

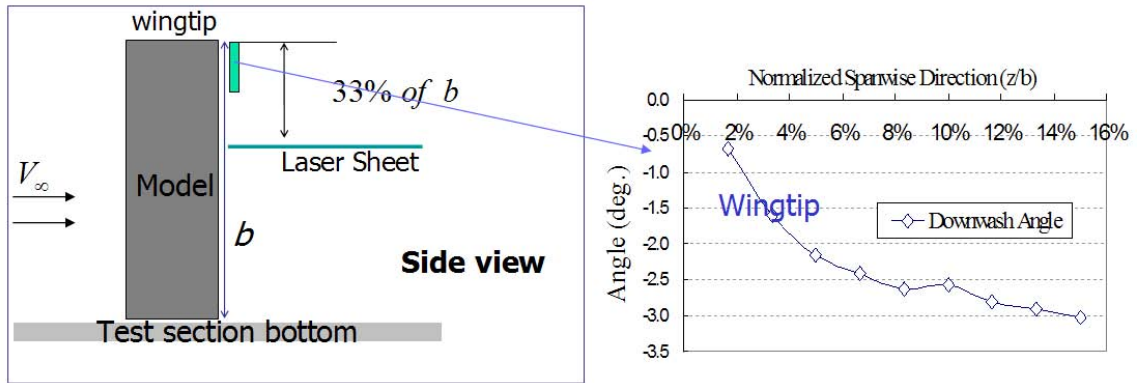


Figure 19 shows representative results from the Trefftz plane PIV showing a portion of the spanwise distribution of downwash from the wingtip to 16% semi-span inboard becoming asymptotic.

5.2 Effect of Changes in Gap

The purpose of this analysis was to study the effect of changes in gap at constant stagger. The results are presented for models of similar stagger. Figure 20, Figure 21 and Figure 22 show the lift curve, C_L , vs. α for varying stagger configurations at a Reynolds Number of 60,000. In all cases, increasing gap increases lift coefficient for a given angle of attack. The change in lift coefficient is higher for negative stagger. At positive stagger this change in lift coefficient is smaller. In particular, for $s = 1c$, after stall, which occurs between angles of attack of 8° and 13° , higher gap models produce less lift. In general the angle of stall doesn't change as a function of gap. It can be seen, however, that increasing the gap increases the slope of lift curve.

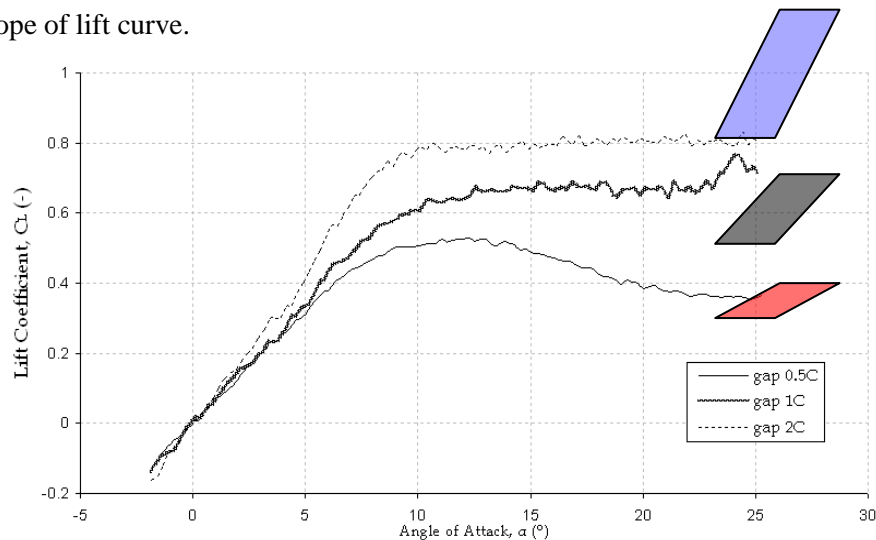


Figure 20 shows that at a negative stagger, lift is a strong function of gap even up to $2c$.

$S = -1c$, $Re = 60,000$.

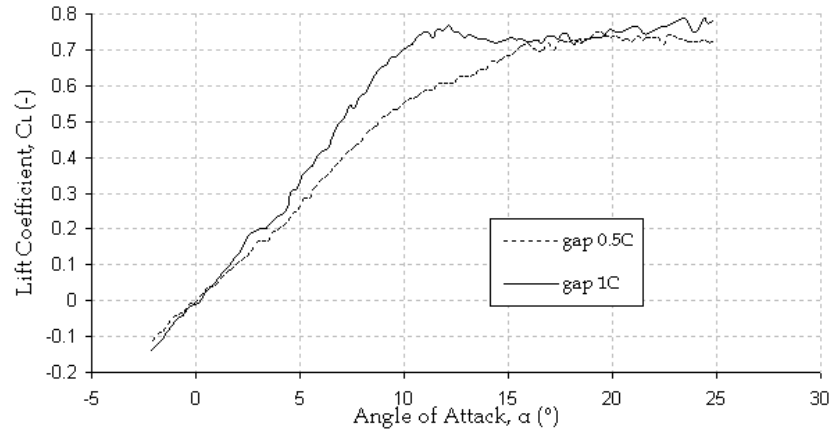


Figure 21 shows there is still some dependence upon gap even at zero stagger.

$s = 0c$, $Re = 60,000$.

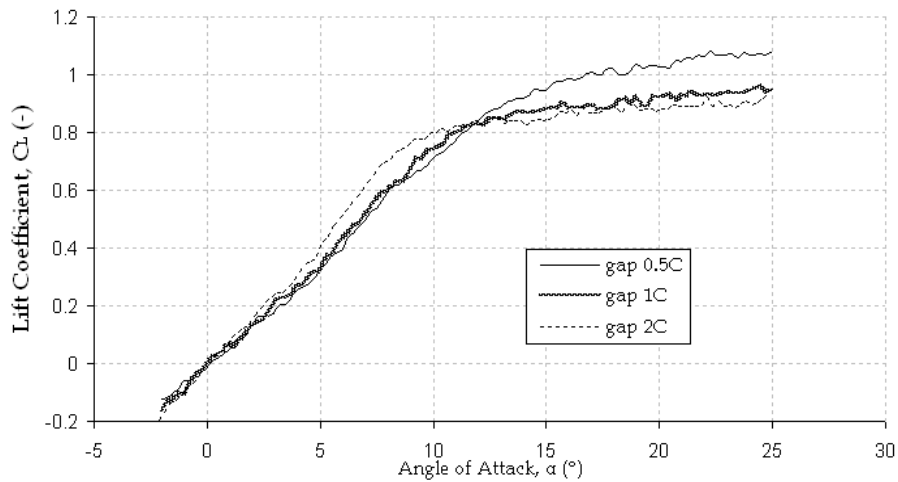


Figure 22 shows much less dependence on gap at a positive 1 chord stagger.

$s = 1c$, $Re = 60,000$.

Figure 23 shows streamwise PIV velocity contours, along with the associated downwash angles for the individual upper and lower wings downstream of the biplane for two different values of gap (0.5c, 1.0c). Once again, it can be seen that the upper wing in both cases generates more lift than the lower wing of equal area and geometric angle of attack. In addition, the greater gap creates greater downwash overall implying more efficient lift production. There was also no discernible increase in velocity between the two wings in the lower gap cases where an increase would most likely be found.

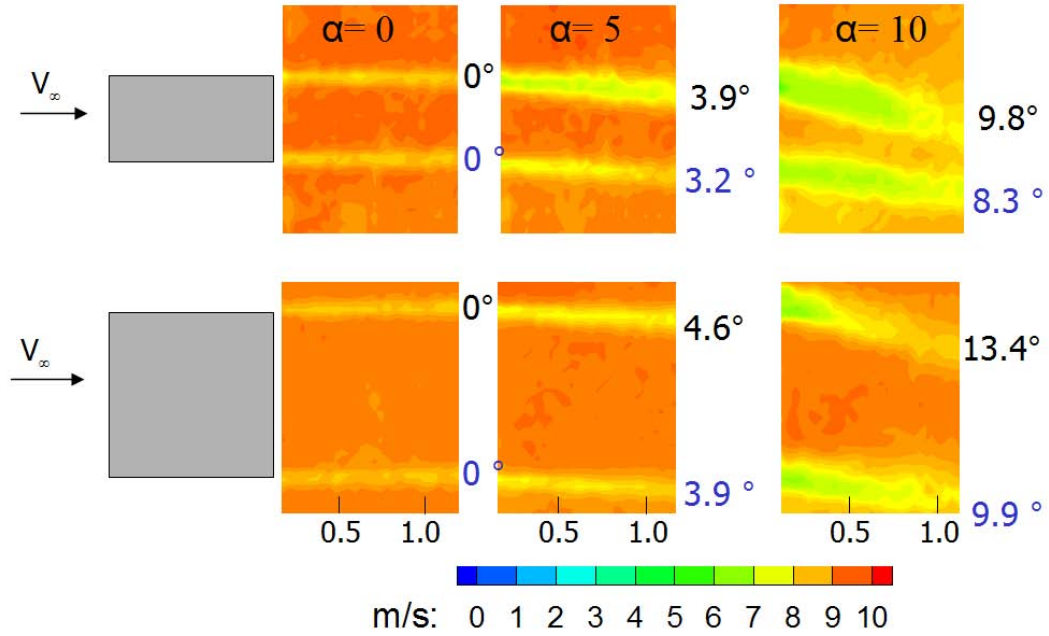


Figure 23 streamwise PIV velocity contours behind two biplanes with different gaps (0.5c, 1.0c) clearly show an increase in downwash angle behind the biplane with greater gap implying greater lift as well. The numbers to the right of each contour figure represent measured downwash angles of the individual upper and lower wings.

5.3 Downwash Relations

Through quantitative streamwise PIV, Figure 18 and Figure 23 have already demonstrated the relative dependence of downwash angle of the individual upper and lower surfaces on gap, stagger and angle of attack. Using:

$$\frac{d\varepsilon}{d\alpha} = \frac{2C_{L\alpha}}{\pi \cdot AR}$$

where AR is constant for all configurations tested for the parametric study in the UD-LSWT, the lift coefficient is directly proportional to the downwash angle. The comparison seen in Figure 24 can be validated by substituting the PIV determined results for $\frac{d\varepsilon}{d\alpha}$. This figure also demonstrates how the disparity between upper and lower surface downwash angles grows with increasing stagger. This disparity appears to improve the lift efficiency as well, as seen by the superimposed lift coefficient results.

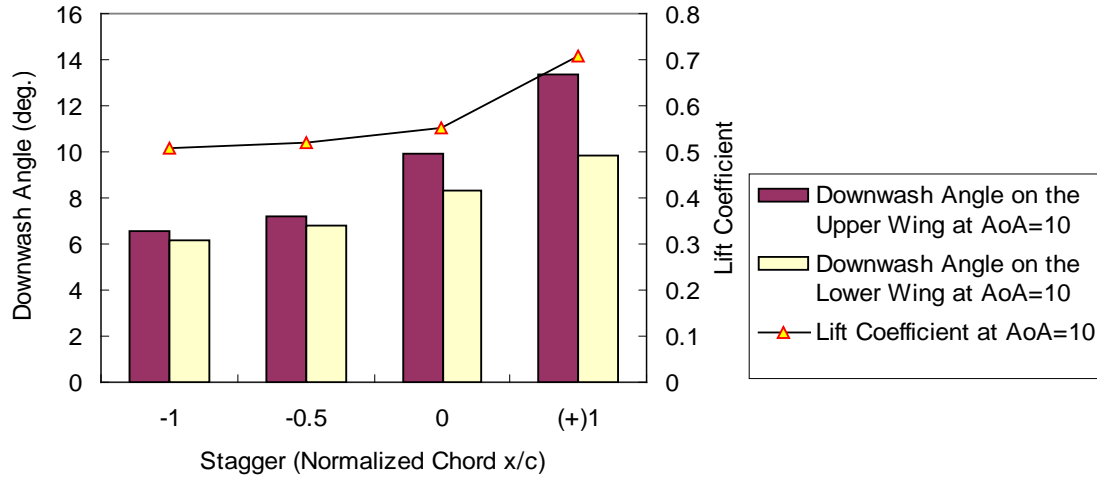


Figure 24 contrasts the downwash angles behind the upper and lower wings as a function of stagger at an angle of attack of 10 degrees with a superimposed integrated lift coefficient demonstrating the proportional relationship that still exists between lift coefficient and downwash.

Another way to look at the same data can be seen in Figure 25. At lower angles of attack, the downwash derived lift coefficients compare quite well to the integrated force derived lift coefficients. At higher angles of attack there are much greater deviations. This is very likely due to separated flow lift enhancement/leading edge suction for several reasons. Firstly, the measured integrated force shows a reduction in lift slope for the negative stagger cases where a pressure deficit would be expected between the lower and upper wings. The force results seen in Figure 17 imply this pressure deficit would propagate upstream and force separation near the leading edge eventually causing lower C_{Lmax} . An example of this leading edge separation bubble can be seen in Figure 26 obtained from Walker [2]. Secondly, in addition to the decreasing C_{Lmax} seen with decreasing stagger, leading edge suction generated lift would not be accounted for in the preceding equation. The greatest difficulty with this assertion is that leading edge suction lift should yield a non-linear lift curve and this is not the case. In addition, if a leading edge separation bubble were responsible for this difference, then a change in Reynolds number should cause some change in lift behaviour. This is also not the case with these results.

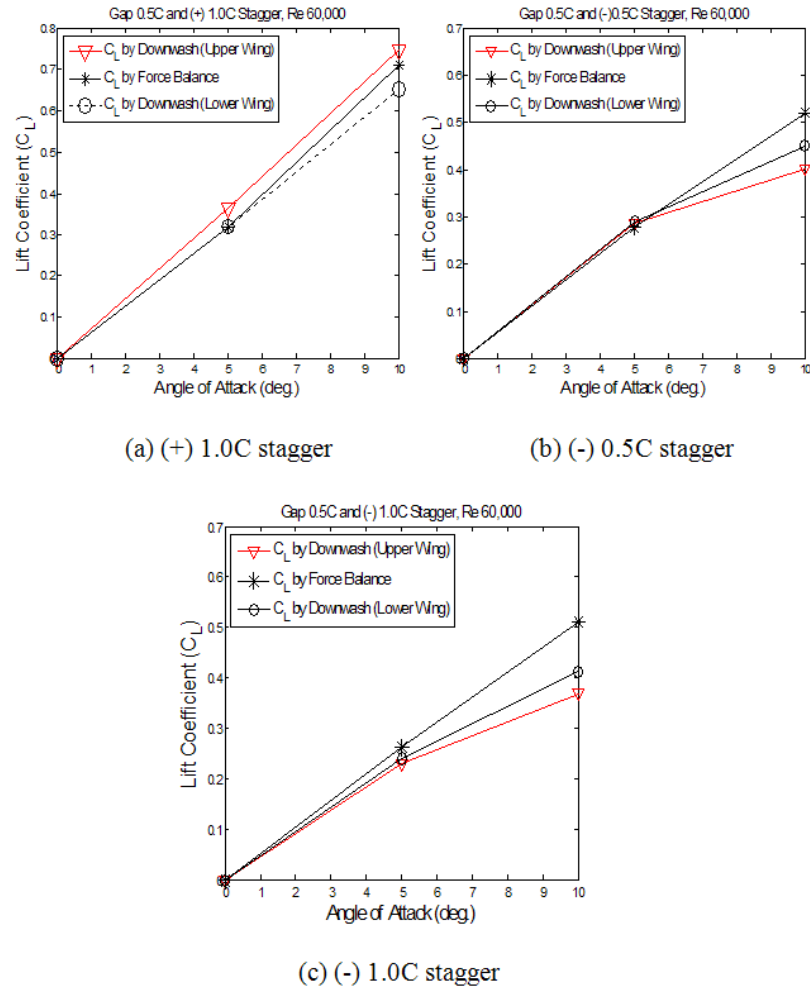


Figure 25 Compares C_L determined through integrated force measurement to C_L calculated from ϵ for the upper and lower wings independently at a fixed gap of 0.5c and various staggers. All stagger cases compare quite well at lower α , but only the positive stagger case compares well at higher α .

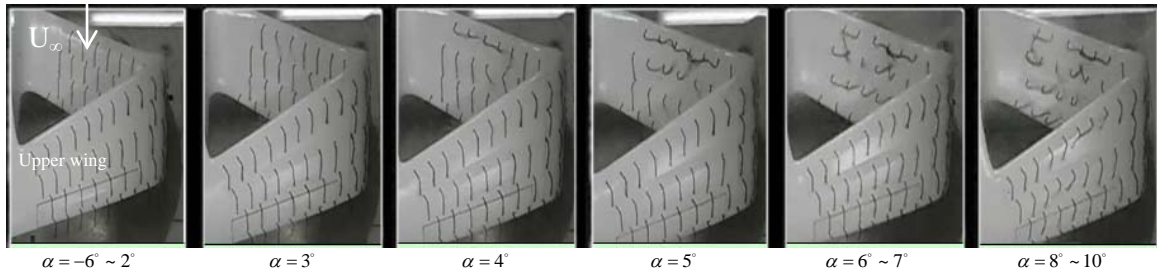


Figure 26 Tuft flow visualization of a 24'' Houck Configuration at 50 mph (Re 215,000): progression of leading edge separation bubble for a positive stagger configuration (reproduced from Walker [2] with zero lift shifted angle of attack).

5.4 Kutta-Joukowski Integrated Circulation Derived Lift

In most cases, the trailing vorticity was diffuse and not well defined due to the presence of the endplate. Despite this diffusivity and the lack of a well-defined trailing vortex, integrating vorticity to obtain circulation and thereby lift behind multiple planar surfaces joined at the tips was reasonably successful. Since the setup time for Trefftz-plane stereo PIV is considerably longer than normal 2-dimensional PIV, a reduced parameter set was tested. These models/parameters were selected because their force results were the most revealing and they were thought to be the models that would benefit most from a detailed flow physics investigation.

5.4.1 K-J Lift: Stagger

Figure 27 compares integrated circulation lift results to integrated force balance derived lift results across a variety of stagger ratios. It is evident that at the lower angles of attack, the circulation derived lift accounts for most of the lift determined through direct force measurement. At values of negative stagger, for the higher angles of attack, the circulation derived lift does not seem to account for all of the lift being measured. In the presence of a leading edge separation bubble, it is unlikely that the circulation being generated at the leading edge would be accounted for through K-J integration of circulation in the Trefftz-plane. These results serve to support the arguments put forth in the downwash section regarding deviations in the measured integrated force lift from the downwash predicted lift.

5.4.2 K-J Lift: Gap

In contrast to some of the stagger results above, Figure 28 shows excellent agreement across all angles of attack between the Kutta-Joukowski derived lift and the integrated force derived lift for both gap ratios at the zero stagger condition. It is once again important to note that despite the nature and complexity of the flow behind multiple lifting surfaces joined at the tips by endplates, that an excellent approximation to the integrated lift is still possible through the integration of circulation in the wake.

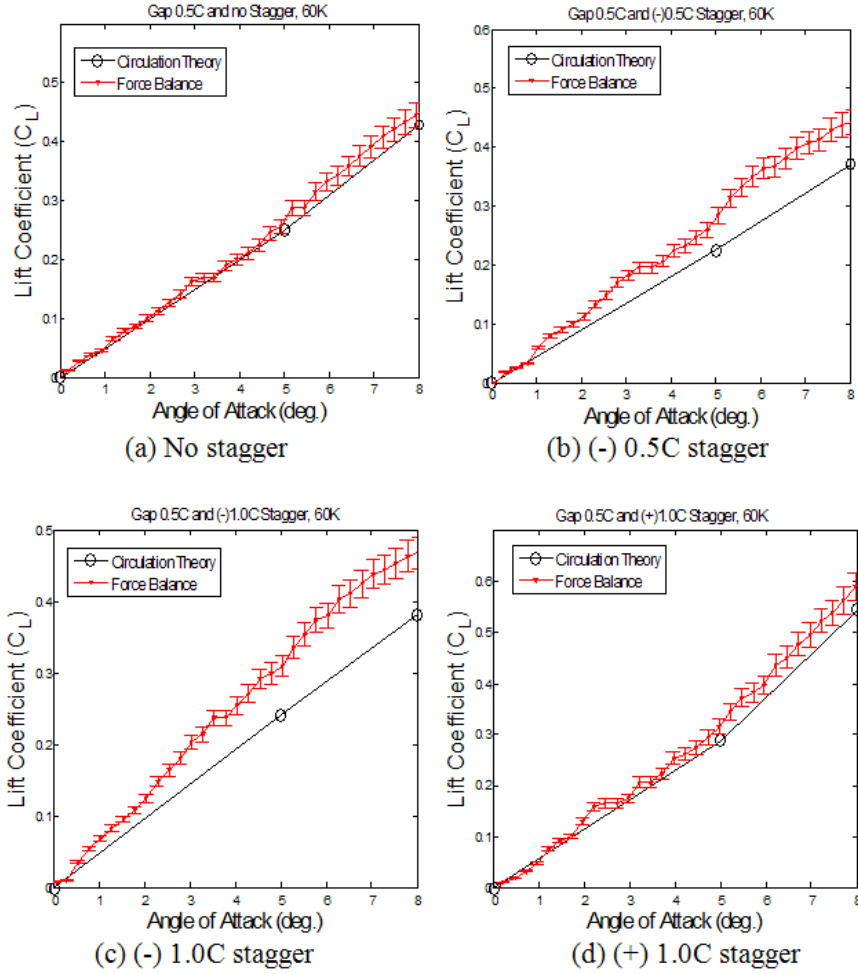


Figure 27 shows that for the zero stagger and positive stagger cases, the K-J derived lift matches the integrated lift force derived results. For the negative stagger cases, the likely cause for the difference is a separation bubble as the suction lift would not be accounted for in Trefftz-plane integration of circulation.

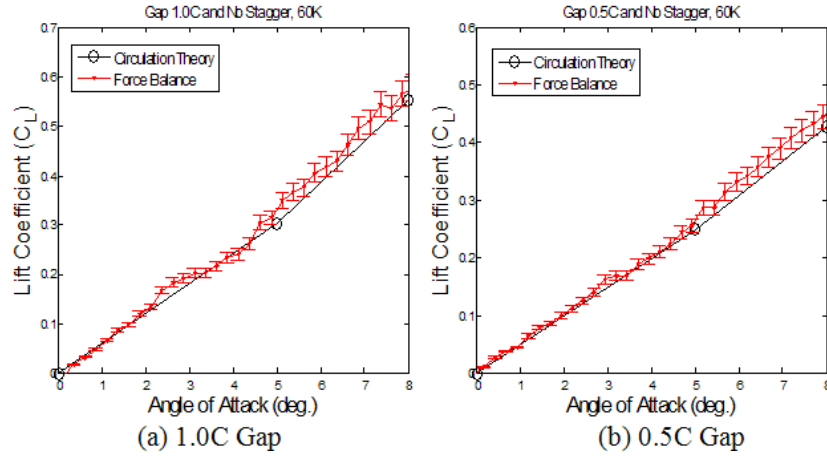


Figure 28 shows that in the case of varying gap with zero stagger, K-J derived lift compares quite well with the integrated force derived lift without any hint of separation seen in the negative stagger cases. It is noted, however, that these lift curves are not well-matched by single linear curve fits.

5.5 Generalized Equation for Biplane Lift

A generalized method for the prediction of lift coefficient as a function of gap, stagger, aspect ratio and angle of attack has been determined empirically and subsequently validated. The development of the generalized equation begins with a linear curve fit for C_L based on varying stagger. Then varying gap was considered in the same manner. The pre-stall C_L data measured by force balance were used to create the generalized equation, to describe the linear lift curves. As explained earlier, the tests in the UD-LSWT showed lift coefficient has a weak dependence on Reynolds number (the difference is less than 2.5% between Reynolds numbers of 60,000 and 120,000 tested). Thus it was considered unnecessary to include the effect of Reynolds number in the generalized equation. Gap and stagger were found to be the most relevant factors in the determination of the lift curve. The results were then adapted to be applicable to any aspect ratio and not only the aspect ratio 6 used in the UD parametric study and subsequently validated against cases run in other wind tunnels with other models.

When these effects are combined from the UD-LSWT data, the resulting generalized equation is:

$$C_L = [((-0.007 \cdot s + 0.015) \cdot g + (0.018 \cdot s + 0.05)) \cdot \alpha] \cdot (-0.0045 \cdot AR^2 + 0.07 \cdot AR + 0.75)$$

Where s is stagger and g is gap. A validation case for the generalized equation can be seen in Figure 29. The Killian/AFIT results compare quite well across the linear range of angle of attack despite the dramatic differences between the Killian configuration and the configurations tested in the UD-LSWT.

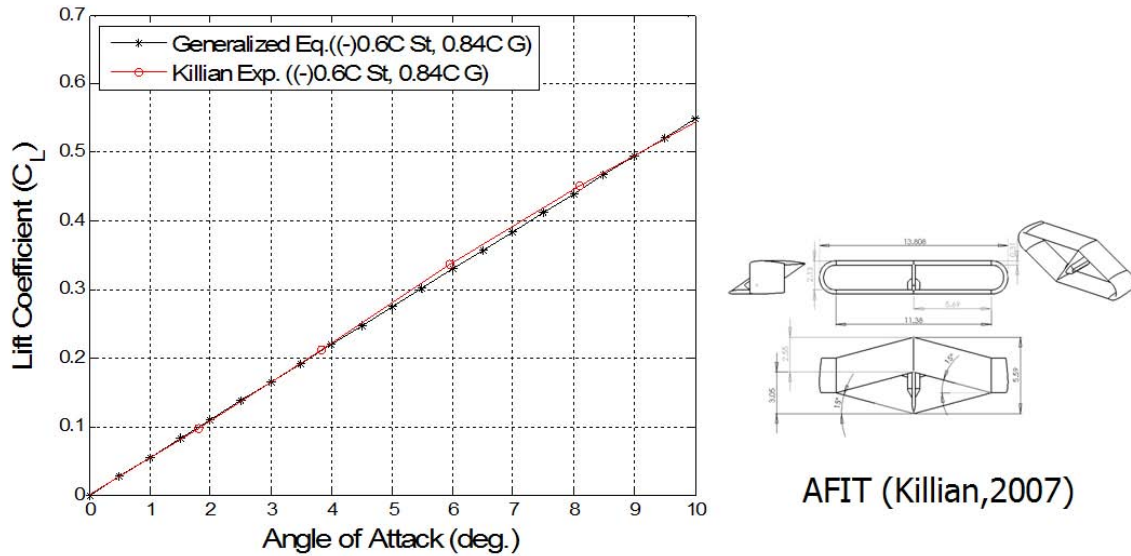
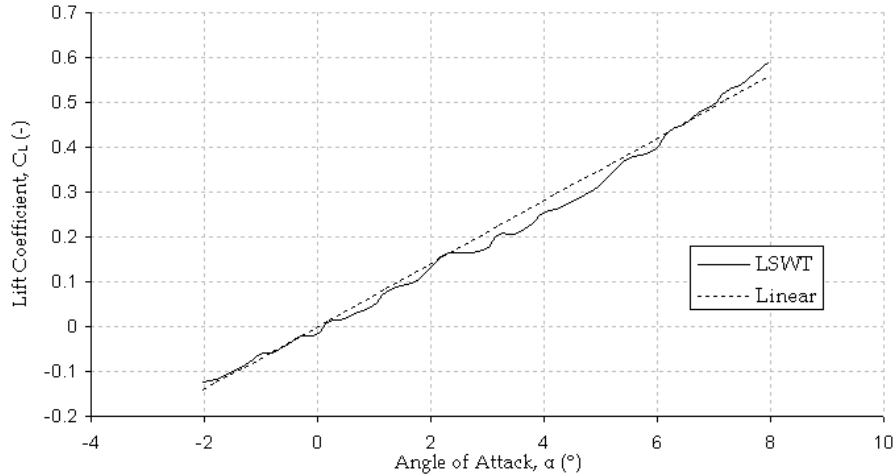


Figure 29 compares the generalized empirical biplane lift equation to a configuration tested at AFIT using a gap and stagger not explicitly used in creating the empirical equation. The AFIT results have been zero lift shifted for the purposes of comparison since they used a NACA 2412 airfoil.

5.6 Change in Lift Curve Slope, or, “The Kink”

Figure 30, a plot of C_L vs. α in the linear regime (angle of attack between -2° and 8°), shows a change in the slope of the lift curve at approximately a 5° angle of attack. This angle of attack where the transition is seen happens to be the same approximate angle where all of the models experience maximum aerodynamic efficiency. This change in lift curve slope was seen for all of the models tested in the UD-LSWT, the University of Maryland wind tunnel, and for many of the AFIT tests. In more closely observing the results from reference [19] from 1929, a kink can also be seen in their lift curves for biplanes even without endplates.



**Figure 30 shows how the lift curve appears to have a departure from a single linear curve fit.
 $g = 0.5c$, $s = 1c$, $Re = 60,000$.**

In determining how the lift slopes were different for a given configuration, C_L vs. α was first plotted in the linear range of angle of attack between -2° and 8° (before stall). It was possible to recognize a region of transition in each of these graphs, where the C_L slope changes from one value to the other. Eliminating this region of transition from the linear curve fits, it was possible to determine a first slope in the region before the transition, and a second slope right after the same transition. In this method, the slope of the first region will be called the inviscid slope and the slope of the second region will be called the viscous slope. Then the percentage change with respect to the inviscid slope is computed. Figure 31 shows a representative lift curve in the range of angle of attack before the transition, and in the range of angle of attack after the transition. For this particular model, the region of transition occurs between 3.22° and 4.72° .

At this point, the reader is reminded of the definition of the angle of stagger provided in Figure 1. It seems that the coefficient of lift slope decreases where there is a large negative stagger angle (see Figure 32). The greatest change in lift slope is associated with the model with the greatest angle of stagger and the lowest change in lift slope is associated with the model with the lowest angle of stagger. Only two models (#8 and #14) do not follow this trend. But it is still reasonable to propose a hypothesis concerning the change in lift slope. It is postulated that increasing the angle of stagger, which can be attained by decreasing the gap or increasing the stagger, creates a positive change in lift slope. This can be translated into a better span efficiency factor after this change has occurred.

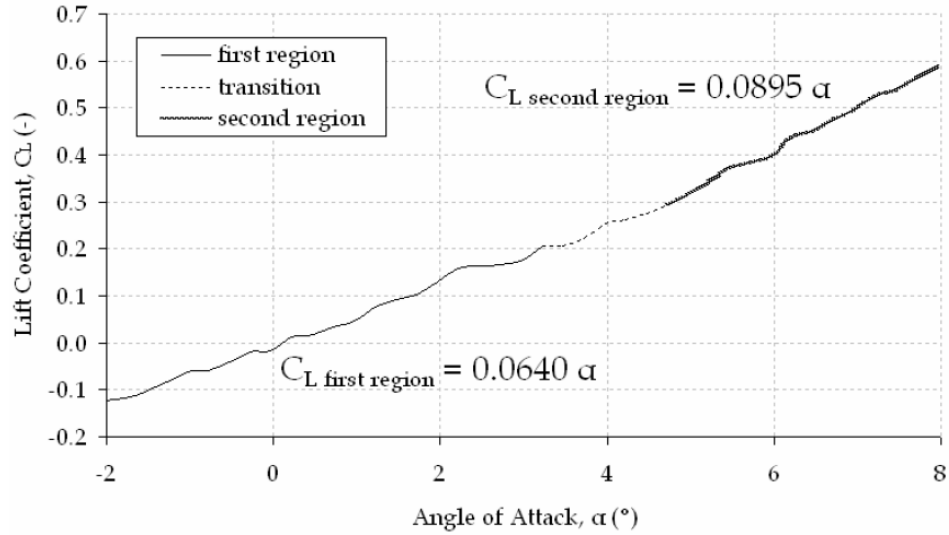


Figure 31 provides one example of the multiple linear curve fits possible when the region of transition is eliminated from the curve-fitting process. This behavior was seen uniformly across all models and Reynolds number tested.
 $g=0.5c, s=1c, Re=60,000$.

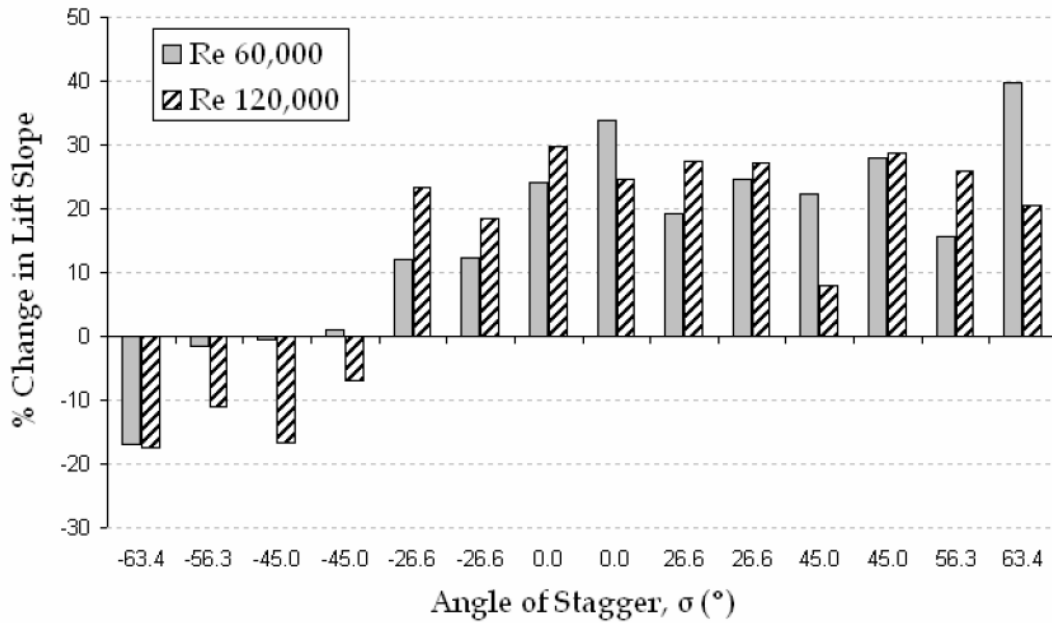


Figure 32 shows that the angle of stagger is the most relevant parameter in determining the magnitude of the change in lift curve slope from region I to region II.

As has already been mentioned, normally a change in lift curve slope is due to separation or suction lift effects. These mechanisms do not typically provide a linear change in lift, especially not

across such a wide range of configurations and conditions. Since there is a certain degree of ambiguity as to the source of this lift curve “kink”, the physics behind the flow were investigated in greater detail using streamwise PIV. It is noted, though, that the same “kink” was also observed in the University of Maryland wind tunnel tests with a single wing (Eppler 423 profile, vs, flat plate and NACA 2412 used at UD and AFIT respectively) and curved endplates. Therefore the phenomenon is not specific to biplanes, a given wing profile, or endplates.

Earlier, it was shown that negative stagger resulted in flow characteristics typical of leading edge separation and suction and the change in lift behavior was not represented by the expected corresponding change in downwash angle. In this instance (see Figure 33) the downwash actually does track the change in lift slope seen in the “kink” suggesting the absence of a similar separated “extra” lift mechanism. The actual mechanism responsible for the step gain in lift and downwash defies explanation using traditional “viscous” arguments.

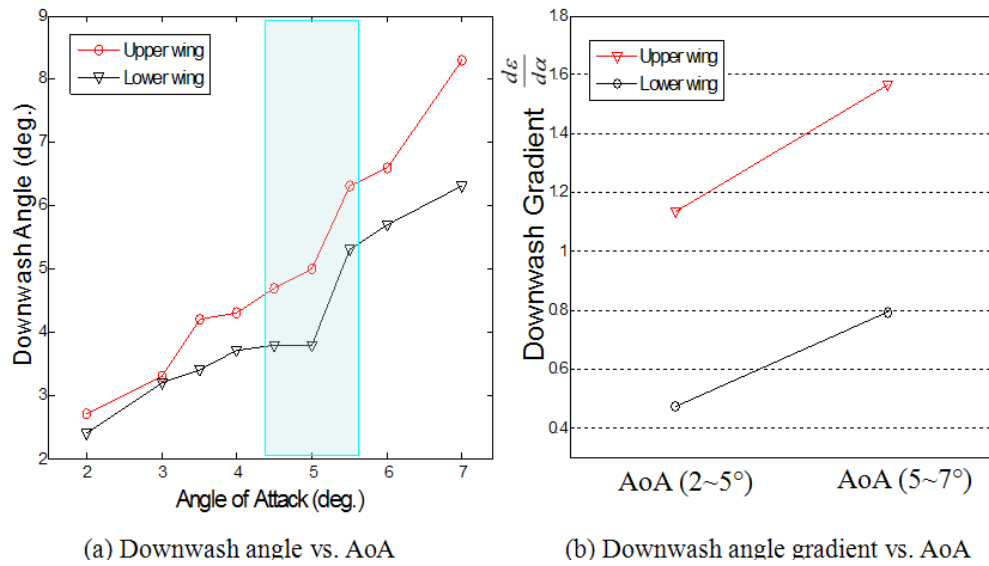


Figure 33 highlights that the change in downwash slope mirrors the change in lift slope in and around the region of transition (or “kink”) as viewed from the perspective of the downwash angle of the upper and lower wings as determined through streamwise PIV.

6 Drag: Experimental Results

6.1 Effect of Changes in Stagger

Figure 34 provides a good example of the type of drag behavior seen from the force balance results. A regular and consistent improvement in lift induced drag is achieved as stagger is increased. Also, there is little discernible difference between the minimum drag of the different configurations tested. At higher values of gap, these differences become smaller and more difficult to distinguish, but the trends are the same. Once again, differences between the two Reynolds numbers tested were negligible.

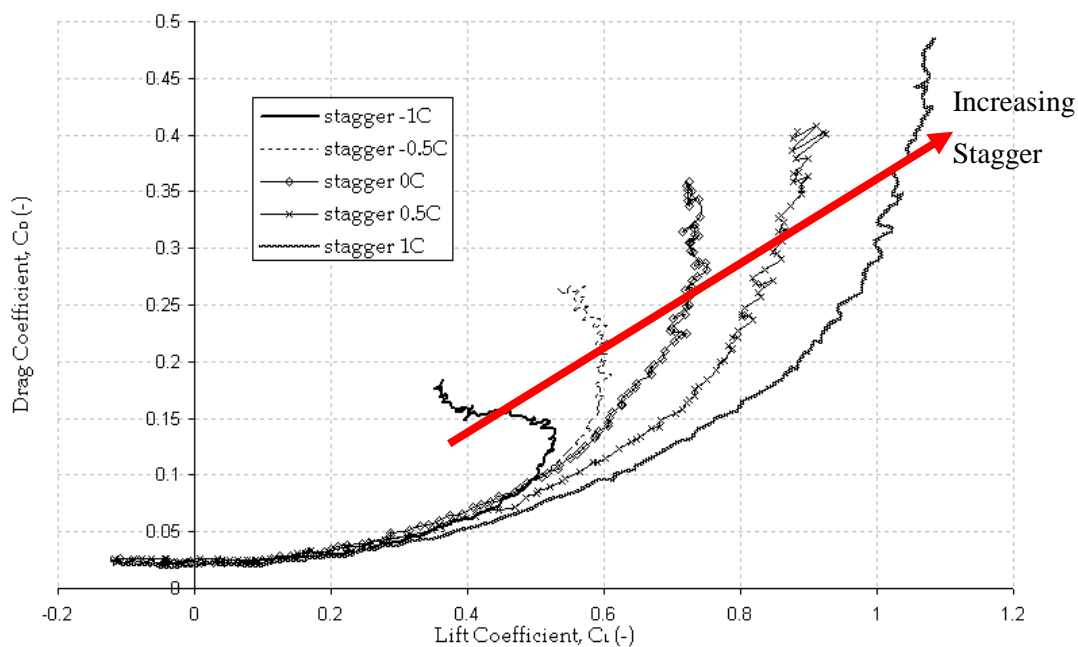


Figure 34 shows that increasing stagger significantly decreases lift induced drag at higher coefficients of lift.

Figure 36 provides phenomenological evidence as to why the lift induced drag decreases with increasing stagger. In the figure, the location and magnitude of the spanwise velocity in the vicinity of the wingtip endplates can be seen to change dramatically as a function of stagger. This in turn affects the wake roll-up and influences both the lift efficiency and the magnitude of the lift induced drag. Figure 36 shows large differences in the vertical velocity around the wingtip as a function of stagger. These results provide some of the strongest evidence that the shape of the wake can be manipulated by the numerous parameters being studied. In this particular case, stagger is the parameter being varied. Changes in stagger also change the rake angle of the endplate. This is an effect that cannot be completely isolated,

although it is believed that the predominant mechanism behind the vastly different shaped contours is the change in stagger and not the endplate rake angle. Endplate rake angle is localized around the tip and it is clear that the dominant effects on the flowfield reach considerably beyond just the wingtip region even in the near wake where the images were acquired.

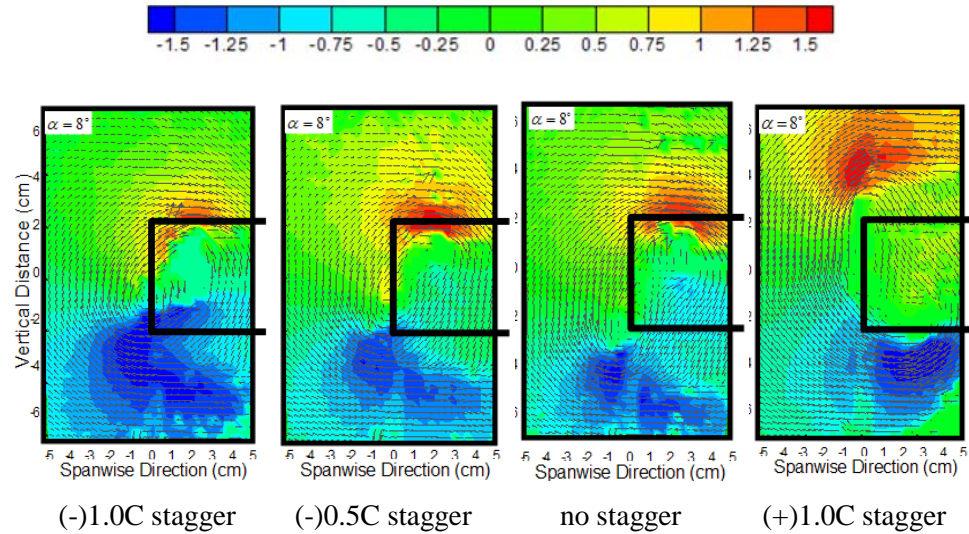


Figure 35 shows how the shape and location of the spanwise velocity in the region of the wingtip changes as a function of stagger. These variations cause fundamental differences in the manner in which the wake rolls up thereby affecting the lift induced drag and the lift efficiency.

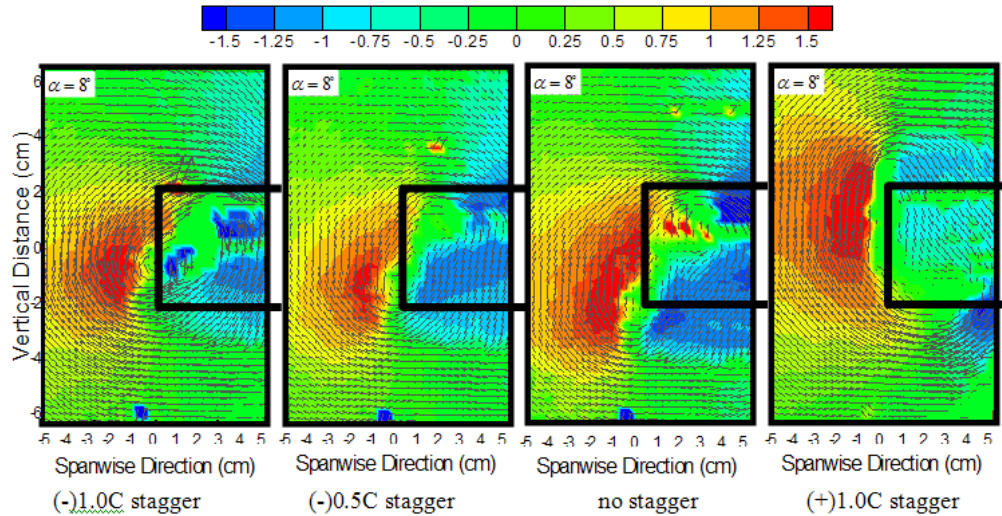


Figure 36 shows how the shape and location of the vertical velocity in the region of the wingtip changes as a function of stagger. Similar to the spanwise variations, these variations cause fundamental differences in the manner in which the wake rolls up thereby affecting the lift induced drag and the lift efficiency.

6.2 Effect of Changes in Gap

A consistent decrease in lift induced drag can be seen with increasing gap and negative stagger in Figure 37. When stagger is positive, however, the same consistent behavior is not seen as in Figure 38 where the 0.5c gap case has the lowest lift induced drag at the highest lift loads.

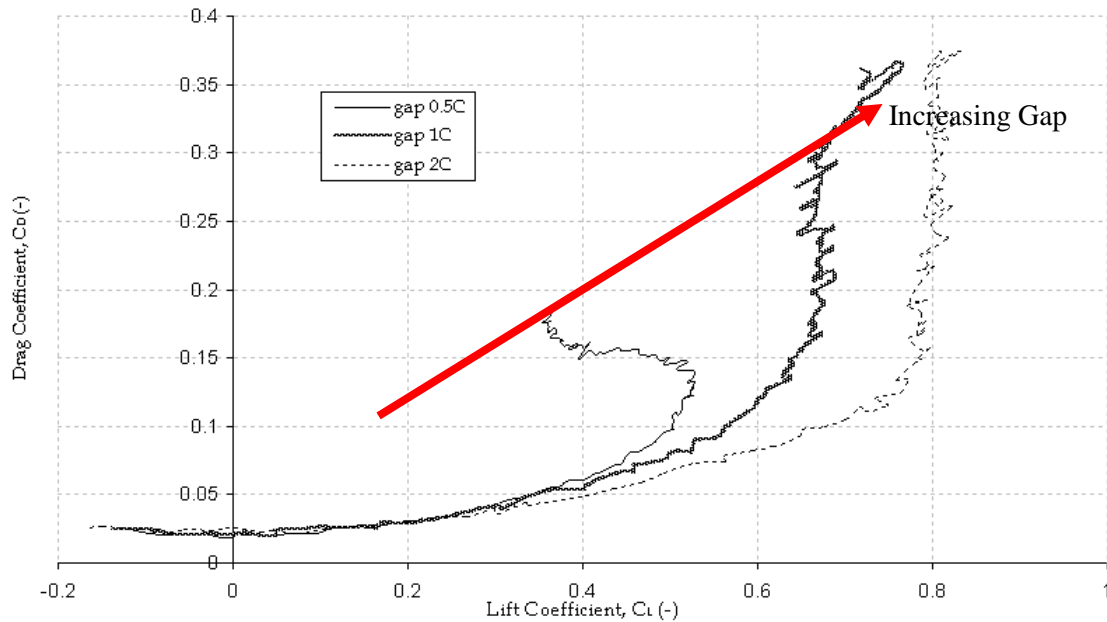


Figure 37 highlights the strong dependence of lift induced drag on gap at a stagger of (-) 1c.

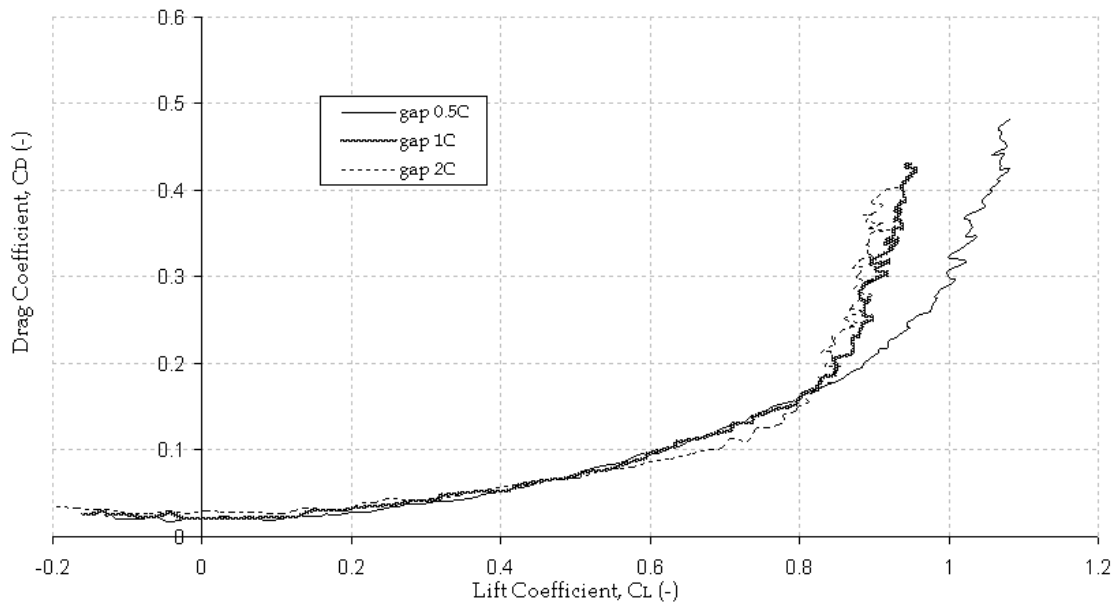


Figure 38 shows that with positive stagger [$s = (+) 1c$] the trend with increasing gap is not consistent in reducing lift induced drag.

Obviously, increasing the gap reduces the region of influence of one lifting surface on another. Thus, the same type of reasoning would be expected to provide insight into why the gap seems to also have a profound effect on the lift induced drag. From a potential flow standpoint, as the distance between the vortices is increased, their expected mutual influence would be reduced. In this instance, the wake is more likely to be broadened in the vertical direction where its effects on lift induced drag would be reduced. Phenomenological evidence of this effect can be seen in both Figure 39 and Figure 40. In Figure 39, the overall contour of vertical velocity is not greatly affected by the increase in gap. If the shapes of the two contours are roughly the same, their relative influence on the shape of the wake and their relative absolute magnitudes would be unequal due to the increased inter-vortex distance. Similar arguments can be made for the spanwise velocity regarding Figure 40.

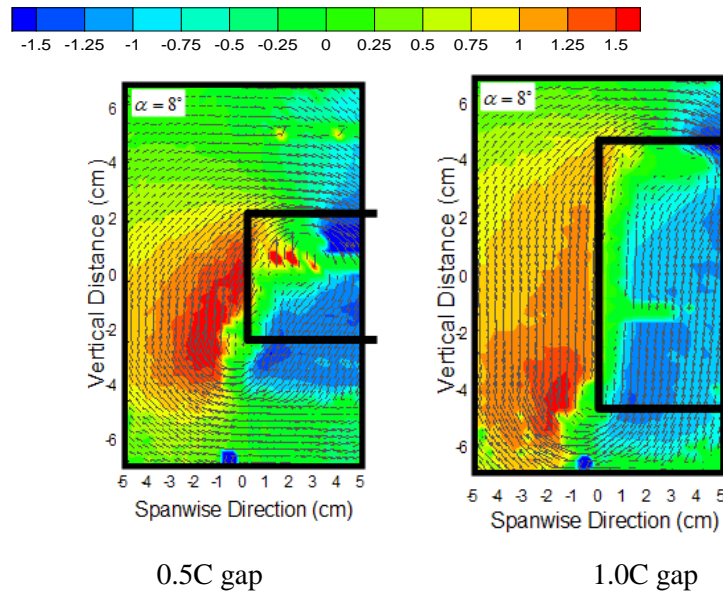


Figure 39 shows that the vertical velocity contours have roughly the same shape in spite of a large difference in gap that corresponds to a large difference in overall lift performance. (zero stagger case).

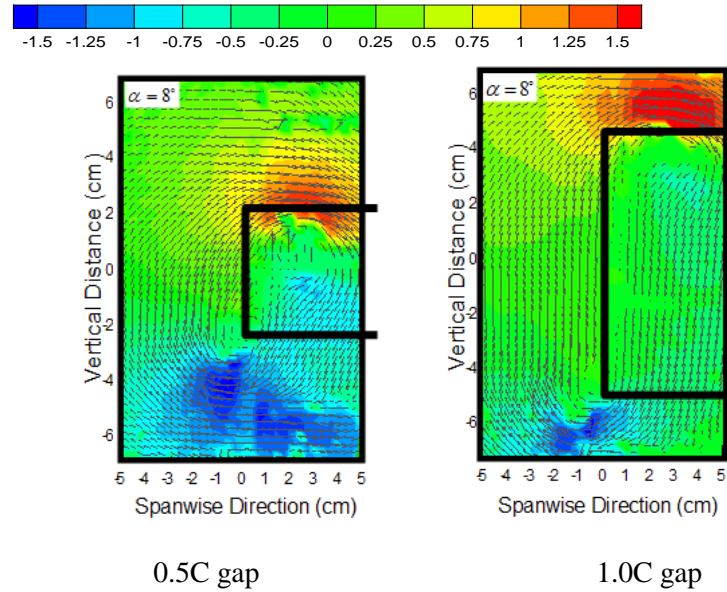


Figure 40 shows the spanwise velocity contours have a strong resemblance despite a large change in gap with a corresponding large difference in lift performance. (zero stagger case)

6.3 Comparing the Orthogonal Biplane and Equivalent Monoplane Models to the Force Balance Results

The theory shows good agreement with the experimental force balance results. In particular, for models without stagger (see Figure 41 and Figure 42), the experimental results match Prandtl's orthogonal biplane theory for $g = 1c$ in the first case, and in the second case where $g = 0.5c$, the experimental results match Munk's equivalent monoplane theory. For staggered models (see Figure 43), Prandtl's orthogonal biplane theory better matches the experimental results. It is no surprise to see the theoretical curves in between the two experimental curves for positive and negative stagger knowing that these theories don't take into account the stagger effect.

Taking a closer look at these three figures, it can be seen that in all the cases the theory matches the experimental curves reasonably well under an angle of attack of four degrees, no matter which theory is used. Once again we encounter the consequences of the "kink" in the lift curves. In this instance, those consequences are relics in the form of increases in lift induced drag associated with the increases in lift curve slope.

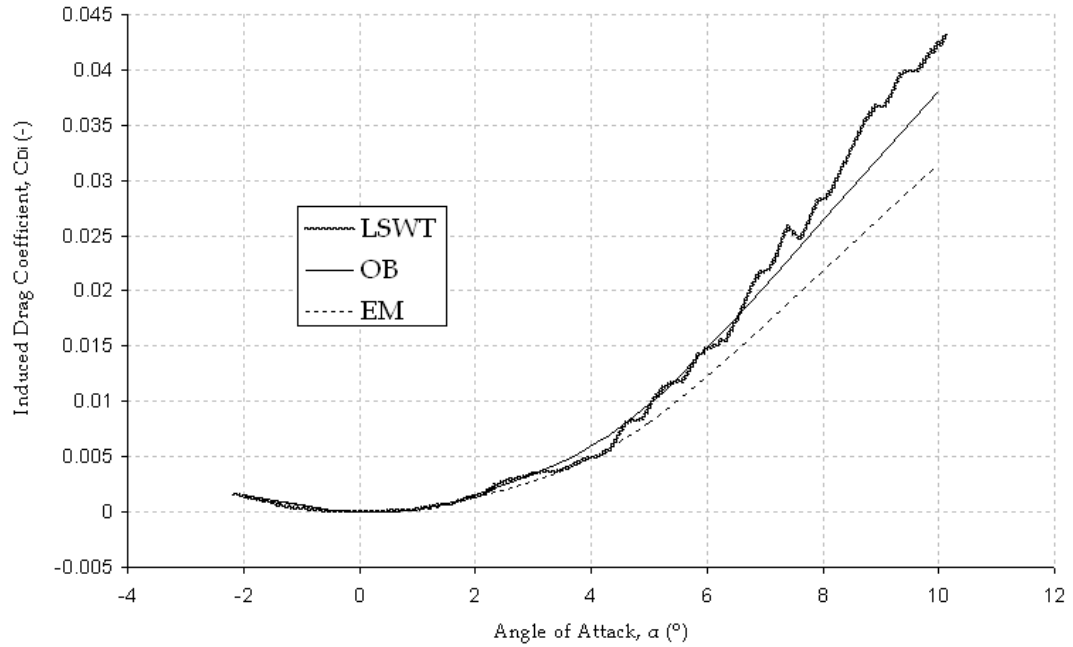


Figure 41 provides an example where the orthogonal biplane model does a good job of predicting the measured drag.
 $g = 1c$, $s = 0c$, $Re = 60,000$.

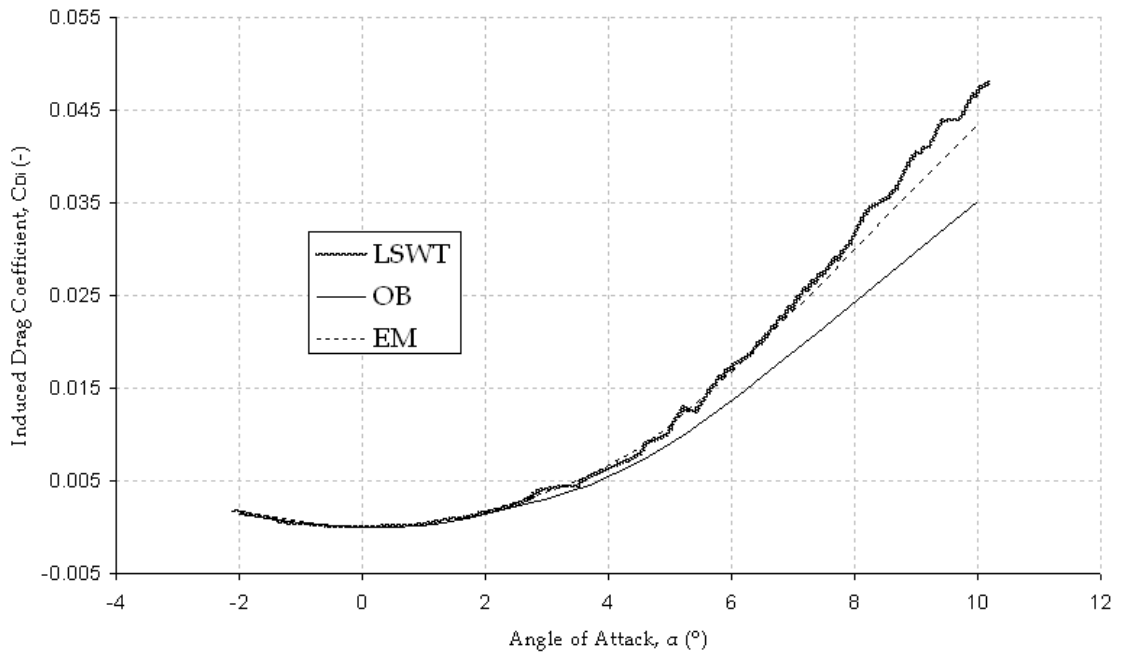


Figure 42 is an example of where the equivalent monoplane model closely predicts the measured drag.
 $g = 0.5c$, $s = 0c$, $Re = 60,000$.

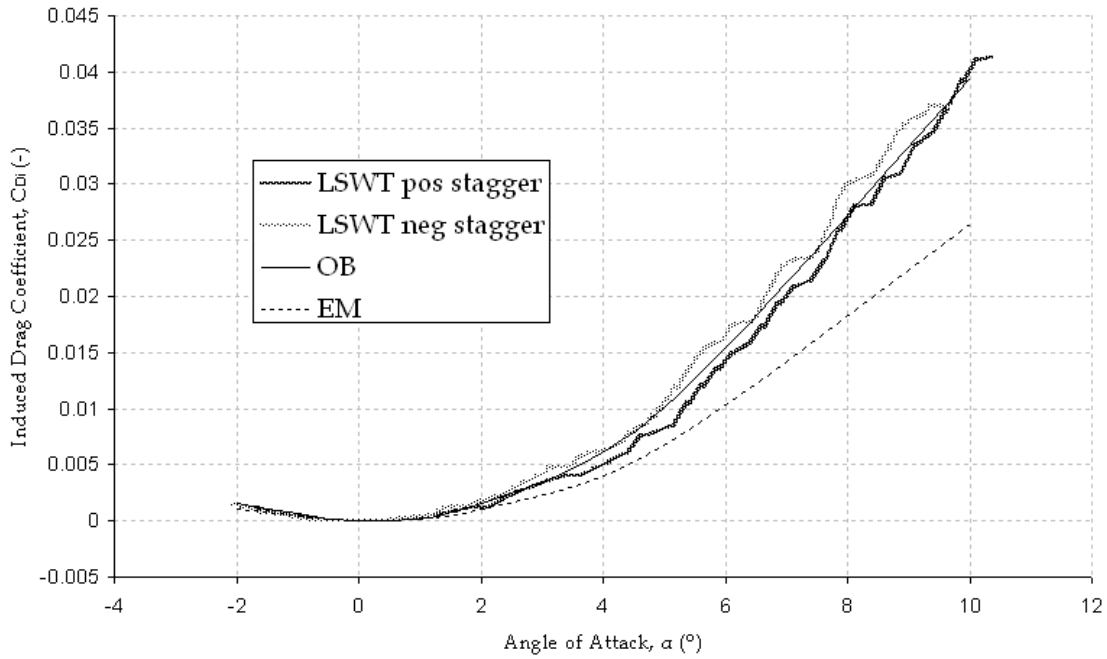


Figure 43 shows the orthogonal biplane prediction falling in between the positive and negative stagger measured drag.

$$g = 1c, s = \pm 1c, Re = 60,000.$$

6.4 Momentum Deficit, Blasius Flat Plate, and Vortex Drag

The agreement between the force balance drag and momentum deficit drag results was expected to be the worst at negative staggers and angles of attack greater than 5 degrees due to the suspected leading edge separation previously discussed in the lift section. The agreement is actually quite good under these conditions. Surprisingly, the greatest deviation between the force balance results and the momentum deficit drag predictions occurs at the lowest stagger and highest angle of attack implying the presence of 3-dimensional flow structures not accounted for in either the wingtip vortex drag or the 2-dimensional momentum integral drag. This only further obfuscates the conclusions drawn previously regarding the lift behavior due to suspected leading edge separation. This result would seem to imply that if there was leading edge separation it was localized to a portion of the span not covered by the streamwise or Trefftz plane PIV. In addition, there was no anomaly in the lift data corresponding to the zero stagger 0.5c gap case that would account for the differences seen between the two drag prediction methods.

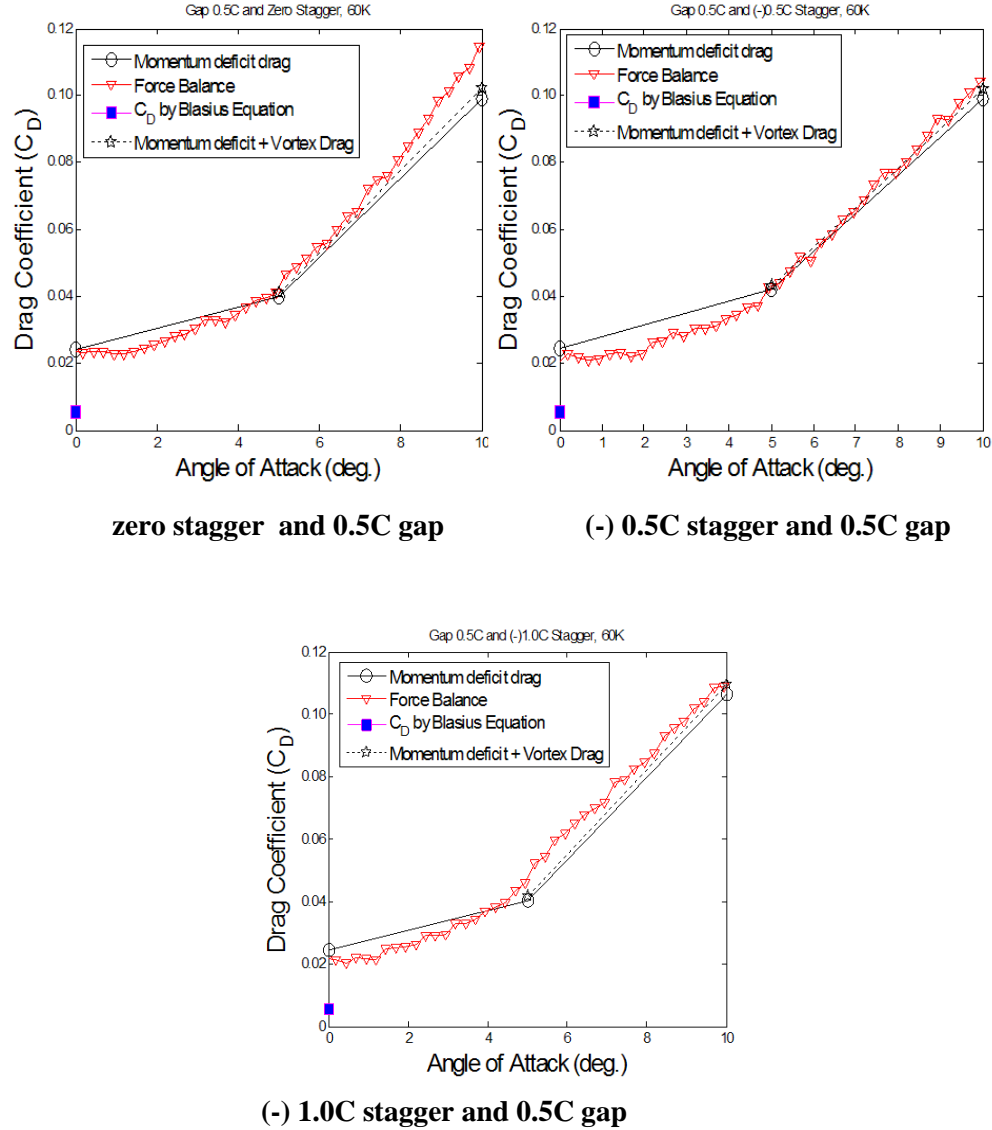


Figure 44 the different drag measurement methods compare extraordinarily well across a variety of staggers.

6.5 Wake Vortex Morphology

Discussion in this section centers on how the wake is shaped by the endplates. The first example can be seen in Figure 45. The figure compares the vertical velocity around two different endplate shapes. Although the stagger and gap are roughly the same for the two models, and the configurations are also roughly loaded equally, the shape and concentration of vertical velocity is fundamentally different between the two examples. The box wing wake is centered more around the lower wing with more shear inboard, whereas the curved endplate wake is rotated considerably higher and closer to the upper wing. The curved endplates cause a smoother transition in the wake from the top to the bottom wings, while a

sharp discontinuity is observed around the flat plate endplates. It should be noted that the curved endplate result did not compare as well to the generalized equation. It was postulated that this was the result of the manipulation of the downwash distribution by the curved endplates.

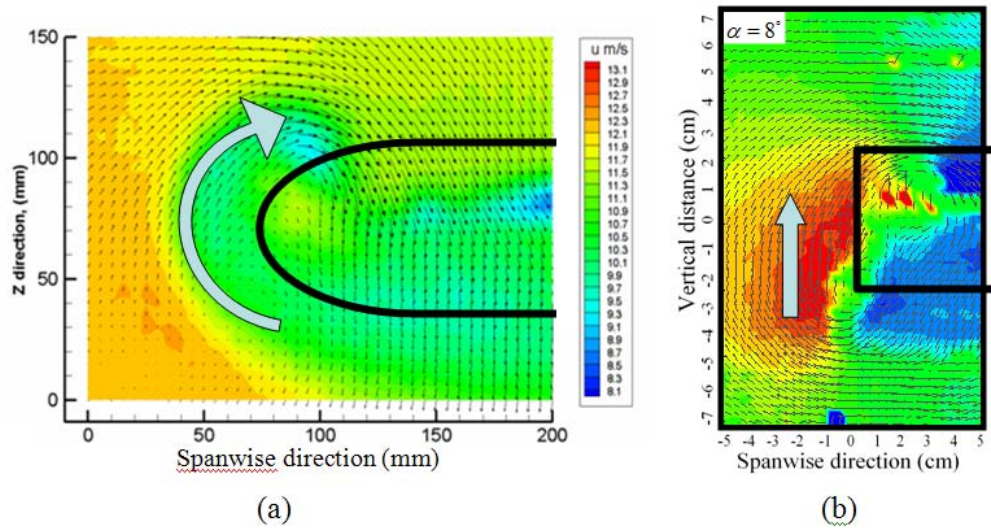


Figure 45 compares the radically different shape of the wake and the vertical velocity field around (a) curved (AFIT, Walker) and (b) flat plate endplates despite the fact that the two wings are loaded roughly the same. Angle of attack in (a) is 10 degrees and (b) 8 degrees.

Figure 46 provides an excellent view of the evolution of the wingtip vortex roll-up downstream. In the near wake, actual tip vortices are difficult to identify in the image. As the wake evolves downstream, distinct tip vortices can be seen, with some ambiguity remaining in the shear layer in the far wake. It would appear, however, from the wake morphology that the greatest concentration of vorticity is aligned with the upper wing, which would correlate well with the findings elsewhere in this report.

Figure 47 is a similar example; however the wings are more highly loaded. In this instance, wingtip vortices are already better defined in the near wake than in the more lightly loaded case and as such, the differences between the near and far wake are more difficult to discern visually. The biggest visible difference is the complete dissipation of the shear layer in the far wake.

Looking across Figure 46 and Figure 47, an evolution of the wake with angle of attack can be seen at each downstream station. In comparing case (a) in both figures, it is clear that the more highly loaded wing has much more clearly defined wingtip vortices, even in the near wake. So it is safe to state that the wake rolls-up more rapidly under higher load conditions as expected.

Figure 48 represents results for a case where the upper/aft wing was replaced with a NACA 0012 wing profile. The results are for a roughly 5 degree angle of attack, and it is clear that the entire shape of

the wake has been changed by the lift offset of the upper wing. There is also little visible difference again between the near and far wake.

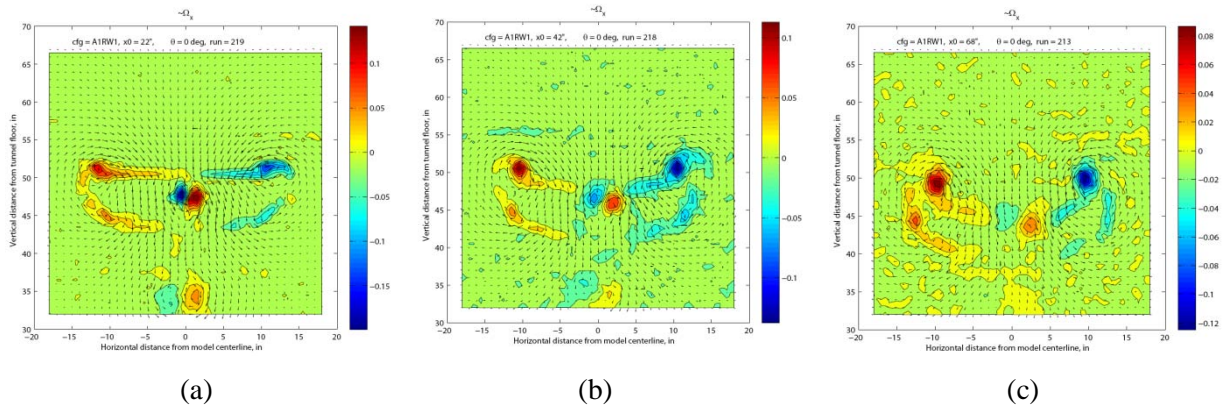


Figure 46 compares the vastly different near and far wake vortex morphology at a roughly 5 degree angle of attack at (a) 22" downstream, (b) 42" downstream, and (c) 68" downstream.

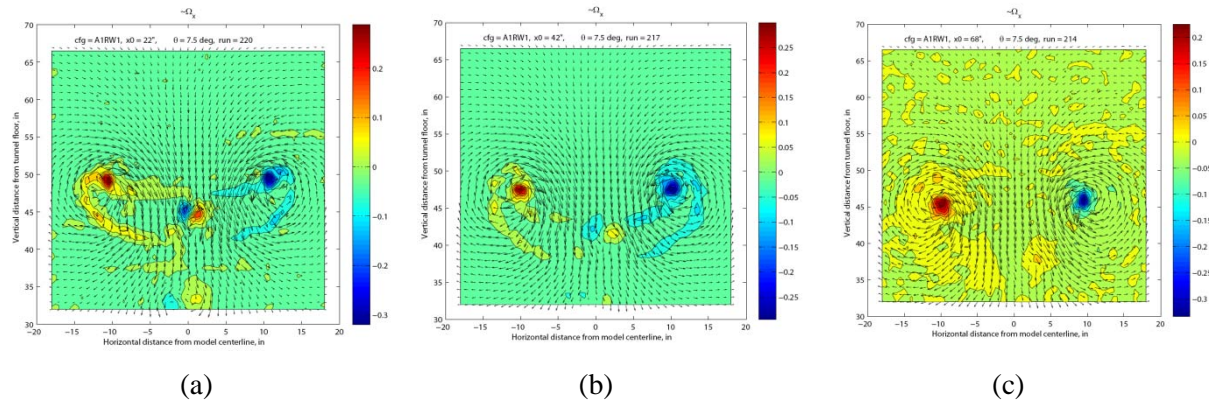


Figure 47 compares the near and far wake vortex morphology in a more highly loaded case where the differences between cases is harder to discern. Roughly 12.5 degrees angle of attack, (a) 22" downstream, (b) 42" downstream, (c) 68" downstream.

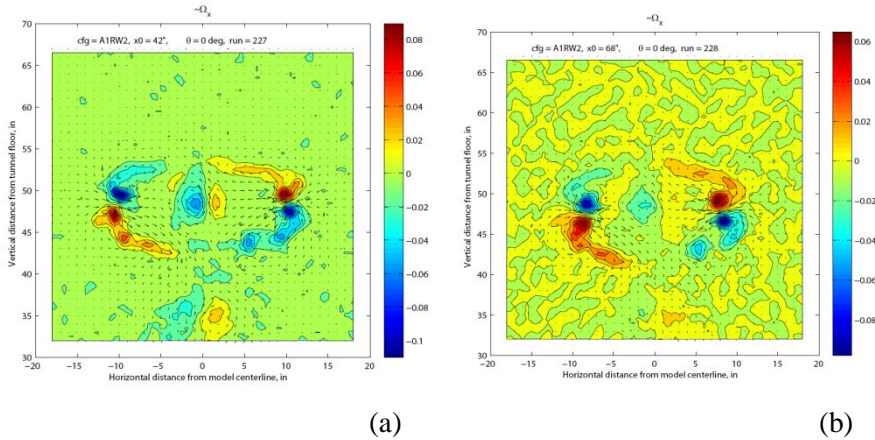
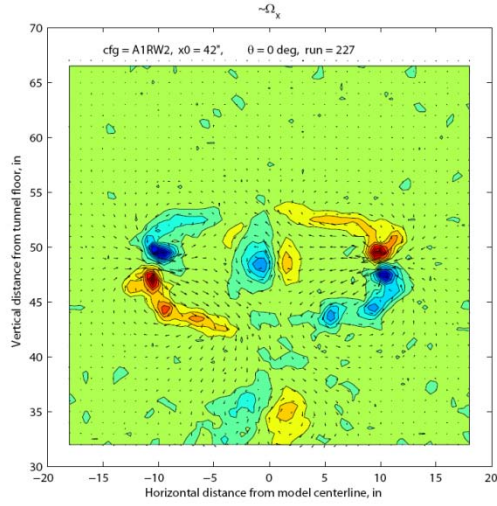


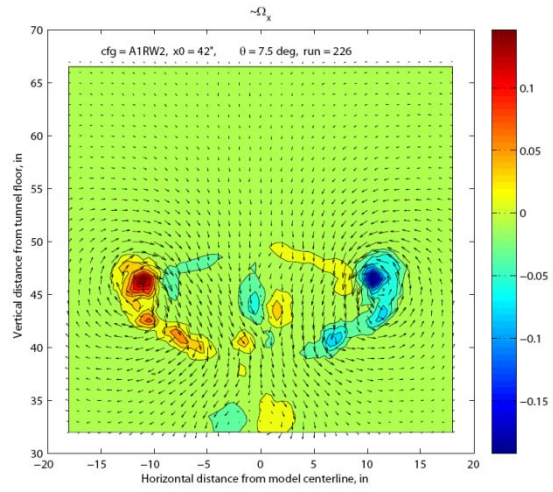
Figure 48 shows that changing the upper/aft wing profile has a significant impact on the shape of the wake in both the near and far wake. ~ 5 degree angle of attack, (a) 42 inches downstream, (b) 68 inches downstream.

Figure 49 uses the NACA 0012 upper wing once again, but this time a comparison can be seen between a more lightly loaded and a more highly loaded case. The effect of the higher loading is clear, as the vortex pairs swallow the shear layer seen at lighter loading. The wake in both cases is still highly curved.

It is important to note that when the “toe-in” angle of the cambered endplates was varied in the experiments by Killian [3] that the configuration that had the highest lift to drag ratio/aerodynamic performance was the configuration with the greatest angle of “toe-in.” This result provides validation of the principle that the targeted broadening of the wake at the same value of lift will provide more efficient lift, and that endplates are an effective manner in which to achieve this.



(a)



(b)

Figure 49 shows drastically different wake morphology between the lightly loaded (a) ~5 degree angle of attack and the more highly loaded case where the vortices merge (b) ~12.5 degree angle of attack and the upper/aft wing has been replaced by the NACA 0012.

7 Design

7.1 Background

The design component of this report is based entirely on the need to define a mission and subsequently conceptually size an air vehicle employing the proposed non-planar configuration in order to determine its performance relative to the traditional monoplane. In order to define this mission, an extensive review of the existing literature was performed to determine the types of missions small UAVs are presently being used to fulfill. The following combination of mission definition, conceptual design and sizing, preliminary finite element structural analysis and preliminary aerodynamic analysis are the result of taking this approach. It is noted that this approach allowed for several iterations through the conceptual sizing process with excellent comparative structural and aerodynamic data as input into the process. This approach yielded a more complete, systems-level comparison of the biplane with endplates along with variation in gap and stagger, to the traditional monoplane.

7.2 Problem Statement

The aim of this portion of the report is to determine if the nonplanar wing under investigation meets the requirements of a Small Reconnaissance Surveillance and Target Acquisition UAV and if so whether there are any structural and/or aerodynamic advantages when compared to a standard “equivalent” monoplane configuration.

7.3 Requirements

7.3.1 Functional requirements

A small, lightweight, affordable man-portable/backpackable and hand launched aircraft capable of providing reconnaissance, surveillance and remote monitoring day and night imagery will be investigated. Such a small reconnaissance plane should be able to loiter about a ground target over a hill or behind a building, without being detected thus reducing the risk of exposing human personnel to harm.

7.3.2 Requirements and design space

- Weight less than 10 lbs
- Assembled in less than 90 seconds
- Hand launched by the operator
- Powered by an electric motor
- Payload: high resolution camera
- Operating altitude 150 m

- Loiter velocity between 12 m/s and 25 m/s
- Endurance greater than 30 minutes

Above, some of the most important requirements for a Small UAV were described. The proposed aircraft must be very light in order to remain portable by a soldier on foot in an urban battle environment and must also be very easy to assemble. The hand launched feature requires a low stall speed that can allow the operator to throw the UAV into the air easily. The electric motor choice aims to keep soldiers from carrying explosive fuel on their backs, to reduce vibrations that can reduce the quality of the images and to reduce the noise in order not to be more difficult to detect. Finally, the loiter velocity is constrained by the camera's parameters and at an operating altitude of 150 m, the maximum velocity to avoid blurry images with current cameras is between 12 m/s and 25 m/s.

Using the constraint equations for a propeller driven aircraft it is possible to create a constraint diagram (Figure 50) that shows the relationship between the power to weight ratio (H_p/W) and the wing loading (W/S) and therefore defines a feasible range of values for the design space based on the aforementioned requirements. The parameters used in these equations are the result of assumptions made taking previous successful designs of Small UAVs into consideration.

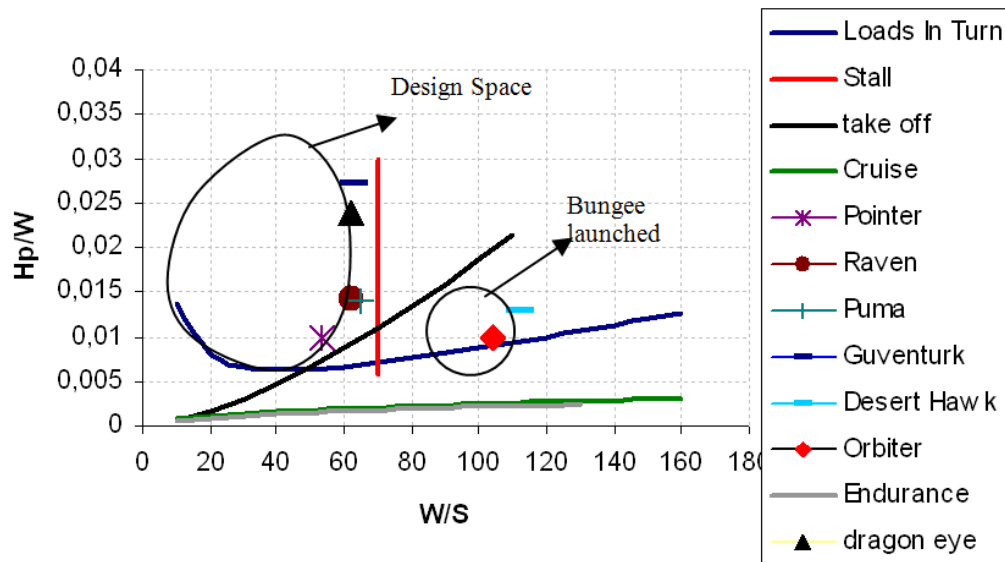


Figure 50 Constraint Diagram defining the design space for a Small UAV with previous designs.

The constraint diagram reported in Figure 50 is important because it shows that any points within the design space represent a possible aircraft design for the required mission based on physics alone. The design points representing some previous successful designs are also reported in Figure 50. The quality of the assumptions made is proven by the fact that all the points that represent the previous designs lie in the

design space with the exception of two of them. Those two outliers represent bungee launched Small UAVs which implies fundamentally different assumptions for stall and maximum lift coefficient.

A sensitivity analysis was also performed in order to study the variation in the size of the design space that can be attributed to discrete variations in the assumptions made.

7.4 Structural Analysis

Using the Finite Element software ADINA to predict stress and displacement, eight structural models were created, whose geometric and physical characteristics correspond to the wing configurations tested in the UD-LSWT (Table 2). The geometric characteristics of the eight models are shown in Figure 51. All of the models have flat plate wing profiles and have identical physical characteristics (Table 3):

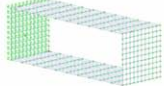

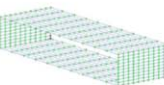

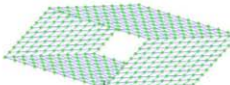

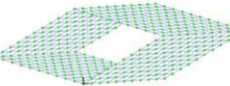

Model #1	Gap 1c Stagger 0c		Model #5	Gap 1c Stagger -0.5c	
Model #2	Gap 0.5c Stagger 0c		Model #6	Gap 1c Stagger 1c	
Model #3	Gap 0.5c Stagger -0.5c		Model #7	Gap 2c Stagger -1c	
Model #4	Gap 0.5c Stagger -1c		Model #8	Gap 1c Stagger -1.5c	

Figure 51 shows the structural models with their geometric characteristics.

Table 3 lists the physical characteristics of the eight models.

c	0.10 m
b	0.60 m
t	1.27 mm
$AR^* = 2b/c$	12
ρ^{**}	8000 Kg/m ³
E^{**}	200 Gpa
ν^{**}	0.3

Under the following assumptions:

1. Elliptical load distribution along the quarter chord of each wing
2. Symmetrical load distribution between the lower and the upper wing
3. Maximum loads determined from a V-n diagram
4. Wing fixed to the wall on one side

the displacements and the maximum effective stresses were calculated and reported in Table 4.

For all of the models, the Maximum Effective Stress reported in Table 4 occurs at the root and the Maximum Displacement at the tip. From Table 4 it can be seen that the configuration with the smallest Maximum Effective Stress is Model #1 with 1c gap and 0c stagger; its stress distribution is reported in Figure 52 in detail using the layout of the software ADINA.

It is also interesting to point out how variation in stagger and gap affects the structural behaviour of the multiple lifting surface configurations under investigation. This effect is clearly illustrated in the Figure 53 where the change in maximum effective stress with variation in the stagger while holding gap constant is reported.

Table 4 calculated displacement and stress for each configuration.

Gap	Stagger	Displacement (m)	Max Effective Stress (MPa)
1	0	0.00904	54.8
0.5	0	0.00868	55.0
0.5	-0.5	0.00897	55.6
0.5	-1	0.01012	57.2
1	-0.5	0.00926	55.2
1	-1	0.01002	56.4
2	-1	0.01032	56.7

1	-1.5	0.0115	58.7
---	------	--------	------

From Figure 53 it can be inferred that increasing the gap and therefore the size of the endplates at the tips of the biplane configuration has a beneficial effect on the structure, reducing the Maximum Effective Stress at the root.

All the models tested in the wind tunnel were fabricated from stainless steel.

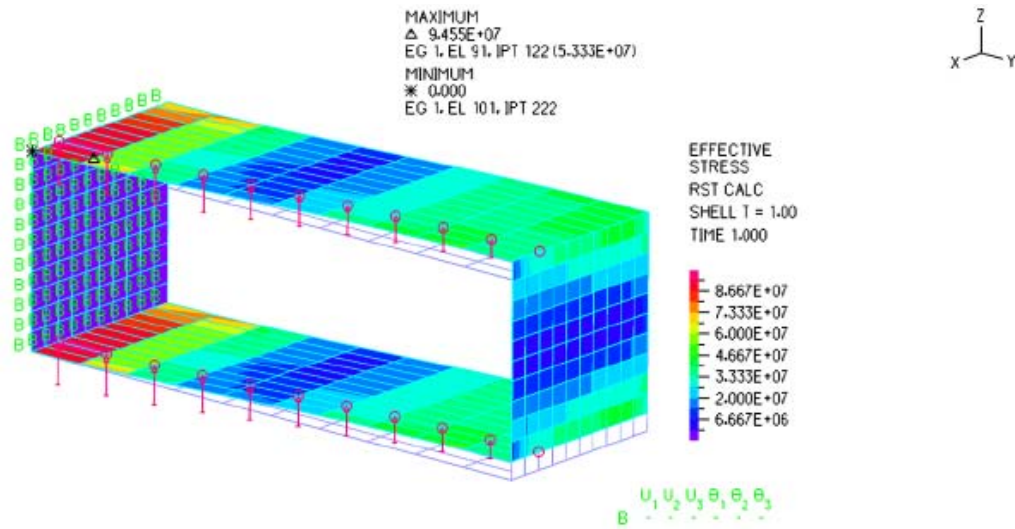


Figure 52 is a screen snapshot of the stress distribution of model #1 with 1 gap and 0 stagger.

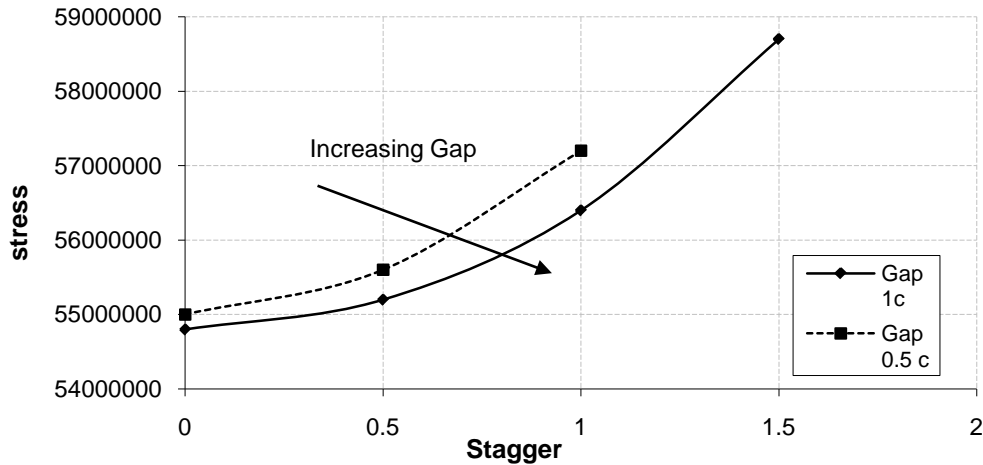


Figure 53 shows the variation in stress due to changes in stagger while keeping gap constant.

7.5 Comparison with the Biplane

In an effort to explore the structural benefits of the use of endplates, eight standard biplane models not joined at the tips with endplates were created using the same finite element software and the results were compared, in Figure 54, to those reported in Table 4 and Figure 53.

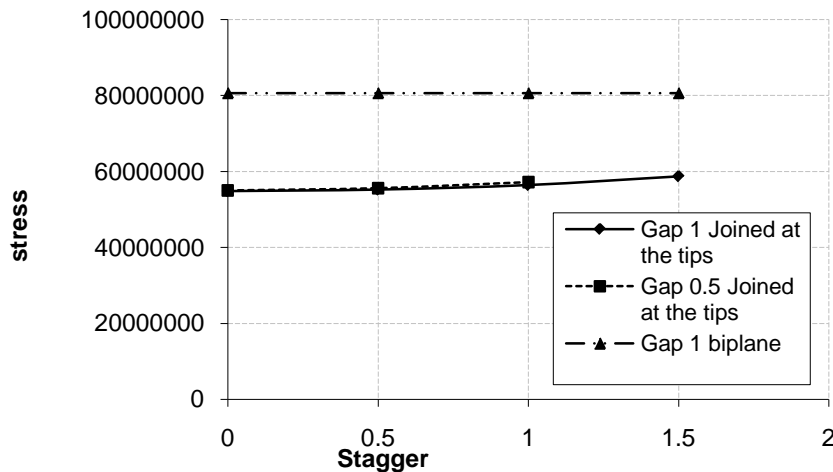


Figure 54 is a comparison of a traditional biplane with no endplates and two biplanes with endplates and different gaps.

As expected, the displacement and the maximum effective stress of the biplane are constant with gap and stagger because the two wings are not joined and therefore they behave independently from one

another. Comparing the maximum effective stress of model #1 with 1c gap and 0c stagger to that of the biplane the reduction in stress is:

$$\Delta\sigma\% = \frac{80,634,000 - 54,800,000}{80,634,000} \cdot 100 = 32.03\%$$

The price to pay for this reduction in stress is the increase in weight of the structure due to the addition of two endplates at the tips. This increase in weight can be easily quantified considering the physical characteristics of the configuration under investigation reported in Table 3, where the same structural material was used in the analysis as was used for the wind tunnel models, stainless steel. Although it is obvious that Stainless Steel would not be used in an aircraft of this type, the wings that were modelled were of constant thickness, and the percentage differences would be the same regardless of the material selected. The weight gain for this particular configuration can be seen as:

$$W_{biplane} = \rho V_{biplane} = 1.22 \text{ Kg}$$

$$W_{endplates} = \rho V_{endplates} = 0.2 \text{ Kg}$$

$$W_{Biplane_with_endplates} = \rho V_{biplane_with_endplates} = 1.41 \text{ Kg}$$

$$\frac{W_{Biplane_with_endplates} - W_{Biplane_with_endplates}}{W_{Biplane_with_endplates}} \cdot 100 = 13.5\%$$

Therefore in order to have a potential reduction in Maximum Effective Stress of 32.03% with a biplane configuration joined at the tips with endplates, there is an increase in weight of 13.5%.

7.6 Comparison to an Equivalent Monoplane

Two different comparisons to an equivalent monoplane are reported in this section in order to understand the potential advantages of using the nonplanar concept under study using different perspectives. Using the same Finite Element software ADINA, a model of an equivalent monoplane was created under the assumptions of:

- The same reference planform surface area (lift capability) between the monoplane and the biplane joined at the tips with endplates
- The same aspect ratio, therefore the same chord but different span:

$$b_{monoplane} = 2b_{biplane_with_endplates}$$
- The same total load
- The same structural material
- Constant thickness along the span and the chord (to simplify modelling)
- Elliptical lift load distribution

In order to have the same Max Effective Stress at the root of model #1 with 1 gap and 0 stagger, the thickness to chord ratio of the equivalent monoplane, using ADINA iteratively, is found out to be 40% bigger than the biplane joined at the tips. The stress distribution for the equivalent monoplane is shown in Figure 55 in detail using the same layout used by ADINA.

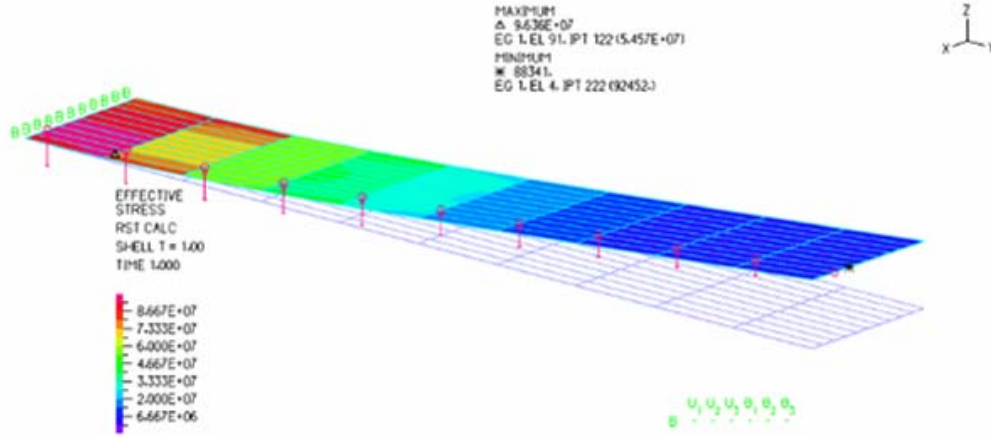


Figure 55 shows the stress distribution of the equivalent monoplane.

The increase in thickness to chord ratio can be considered an estimate of the increase in weight of the structure and it can be easily quantified considering the physical characteristics of the configuration under investigation reported in Table 3:

$$\frac{W_{monoplane_40\%thickness} - W_{Biplane_with_endplates}}{W_{monoplane_40\%thickness}} \cdot 100 = 30.7\%$$

Therefore the consequent potential reduction in weight using the biplane configuration joined at the tips with a 1c gap and 0c stagger is around 30%.

The stall constraint is used to consider the subsequent impact on a vehicle performance constraint:

$$\frac{W}{S} = \frac{\rho_{SL}}{2} C_{LMAX} V_{stall}^2$$

This potential reduction would translate into a lighter aircraft with a reduced stall speed and a longer endurance, all major factors for the mission profile of a Small Reconnaissance Surveillance Target Acquisition UAV. In fact solving the stall constraint for V_{stall} , a reduction in weight of 30%, under the further assumption of the same C_{Lmax} , yields a reduction in the V_{stall} of 19%. Since the target V_{stall} for the design of the Small UAV is 9 m/s, this reduction would lead to a stall velocity of 7.30 m/s.

Given the aforementioned electric propulsion, the following relationship exists:

$$P = IV = TV = DV = \frac{1}{2} \rho V^2 S (C_{Do} + C_{Di}) V$$

and

$$C_{Di} = \frac{C_L^2}{\pi e AR}$$

which yields:

$$P = IV = TV = DV = \frac{1}{2} \rho V^2 S \left(C_{Do} + \frac{C_L^2}{\pi e AR} \right) V$$

Adding that in cruise:

$$C_L = \frac{2W}{\rho V^2 S}$$

The relationship between the power and the weight can then be derived:

$$P = IV = \frac{1}{2} \rho V^3 S C_{Do} + \frac{1}{2} \frac{\rho V^3 S}{\pi e AR} \frac{4W^2}{\rho^2 S^2 V^4} = \frac{1}{2} \rho V^3 S C_{Do} + \frac{2W^2}{\pi e AR \rho V S}$$

Using the same parameters used for the constraint equations in the Requirements section, the resulting power required in cruise is $P = 72$ W. Considering a combined motor and propeller efficiency of 0.6 [21], the power consumed in cruise is $P = 120$ W.

This is a reasonable value when compared to typical values of power required in cruise for a Small UAV previously reported [22]. Using the electric motor AXI 2826/12 [3], with an operating voltage of 11.1 V, and using a Lithium Polymer battery with 3 cells in serial and 4 in parallel with a capacity of 8,000 mAh, the endurance associated with this power in cruise is: ~44 mins.

Considering now the potential reduction in weight of 30% using the biplane joined at the tips with endplates, the required power would be, considering all other parameters constant: $P = 113.56$ W.

Therefore, endurance is computed to be:

$$I = \frac{P}{V} = 10.23 \quad A = \frac{C(mAh)}{h} \rightarrow h = \frac{C(mAh)}{I} = 0.78 \quad h = 47 \text{ mins}$$

While the endurance associated with 120 W was 44 m. In other words a reduction in weight of 30% would produce an increase in endurance equal to 6.4%.

Using the same Finite Element software ADINA, a model of a second equivalent monoplane was created using the assumptions

- The same reference planform surface area (lift capability) between the monoplane and the biplane joined at the tips with endplates
- The same span: $b_{monoplane} = b_{biplane_with_endplates}$ and therefore different AR
- The same total load
- The same structural material
- Constant thickness along the span and the chord
- Elliptical lift load distribution

In order to have the same Maximum Effective Stress at the root as model #1 with 1c gap and 0c stagger, the thickness to chord ratio of the equivalent monoplane, using ADINA iteratively, is determined to be 17% larger than that of the biplane joined at the tips. The stress distribution for the equivalent monoplane is shown in Figure 56 in detail using the same layout used by ADINA.

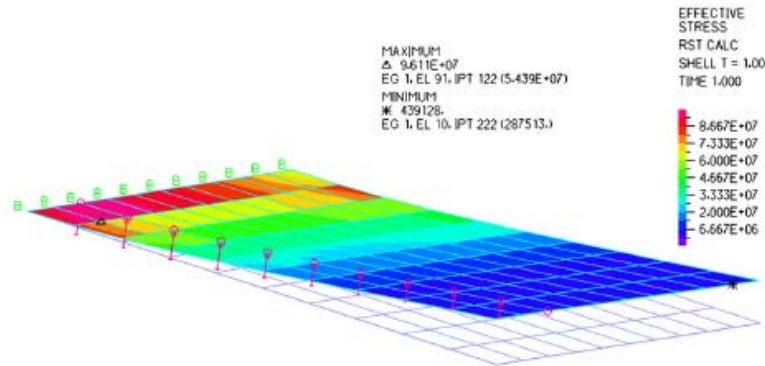


Figure 56 shows the stress distribution of the equivalent monoplane with same span as the biplane (thus, lower effective aspect ratio).

This increase in thickness to chord ratio translates again into a reduction in weight:

$$\frac{W_{monoplane_17\%thickness} - W_{Biplane_with_endplates}}{W_{monoplane_17\%thickness}} \cdot 100 = 3.5\%$$

This weight reduction can be used again to reduce the stall speed or to increase the endurance or, alternatively, to carry a heavier payload. This could be a bigger camera with better resolution or the same resolution but less expensive.

The biplane joined at the tips with endplates with 1c gap and 0c stagger, that gave the smallest maximum effective stress can now be compared to the equivalent monoplane just considered. The aim is always to examine different perspectives regarding the potential advantages of using a nonplanar concept.

7.7 Aerodynamic analysis

Using the vortex panel code software AVL (Athena Vortex Lattice) under the incompressible, inviscid, irrotational and steady flow assumptions, an aerodynamic model of the equivalent monoplane considered at the end of the last section was created (see Figure 57). The geometric and physical characteristics are as follows:

Chord: $c = 0.2$ m

Span: $b = 0.6$ m

Reference planform area: 0.12 m^2

Flat plate airfoil sections

$Re = 60,000$.

The results from AVL for the monoplane were then compared with the results from the UD-LSWT for the biplane joined at the tips, 1c gap, 0c stagger. Figure 58 shows a comparison of the lift slopes of the two configurations. The lift slopes of the biplane joined at the tips and the monoplane are 0.07204 and 0.05424, respectively with a consequent gain in lift slope for the biplane joined at the tips:

$$\Delta \frac{dC_L}{d\alpha} = 24.7\%$$

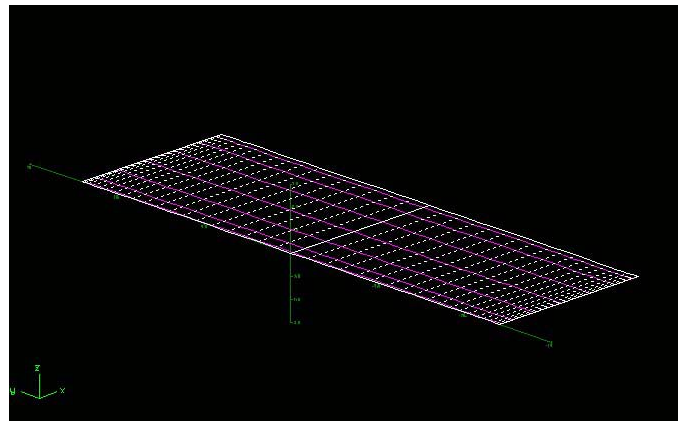


Figure 57 is an example of the Equivalent Monoplane model created with AVL.

It's important to note that this considerable gain in lift slope is in part due to an unusual change in the lift slope of the biplane with endplates that can be observed around 5° . Further investigation is required to better understand this previously discussed unusual behavior. Considering the linear part of the lift curve until 5° , the lift slope is equal to 0.065 with a gain in lift, in this case, equal to

$$\Delta \frac{dC_L}{d\alpha} = 16.5\%$$

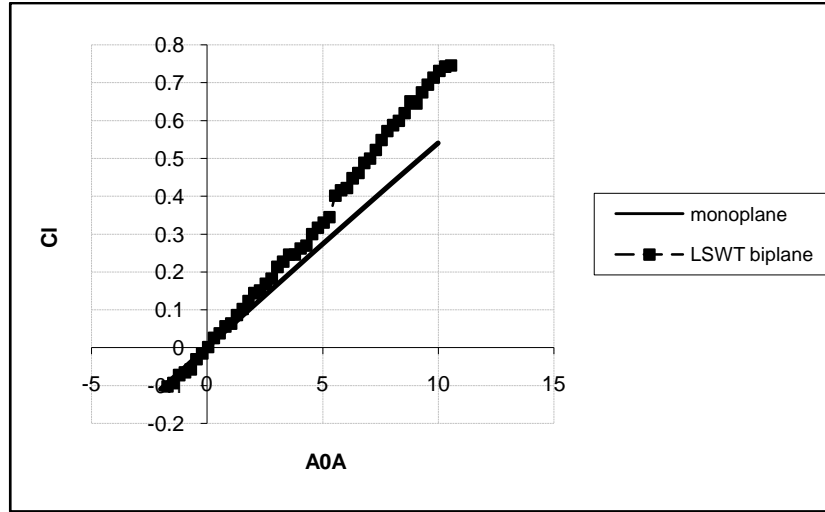


Figure 58 compares the lift curve generated using the UD-LSWT experimental data for the biplane configuration with endplates to the AVL results for the monoplane.

Figure 59 shows the variation of the lift to drag ratio with the angle of attack for the two configurations under consideration. For small values of angles of attack, from 0° to 4° , the biplane configuration shows better aerodynamic efficiency. In particular, this research focuses on the mission profile of a Small Reconnaissance UAV. Therefore, considering its proposed physical characteristics with a takeoff weight of 2.9 Kg and a reference wing planform area of 0.5 m^2 , for a cruise speed of 18 m/s, a design C_L of 0.28 can be calculated. The angle of attack that corresponds to this flight configuration, using a flat plate wing profile, would be 2.56° . The gain in lift to drag ratio for this particular angle of attack would be:

$$\Delta \left(\frac{L}{D} \right) = \left(\frac{L}{D} \right)_{\text{biplane}} - \left(\frac{L}{D} \right)_{\text{monoplane}} = \frac{7.71 - 6.38}{7.71} = 17.25\%$$

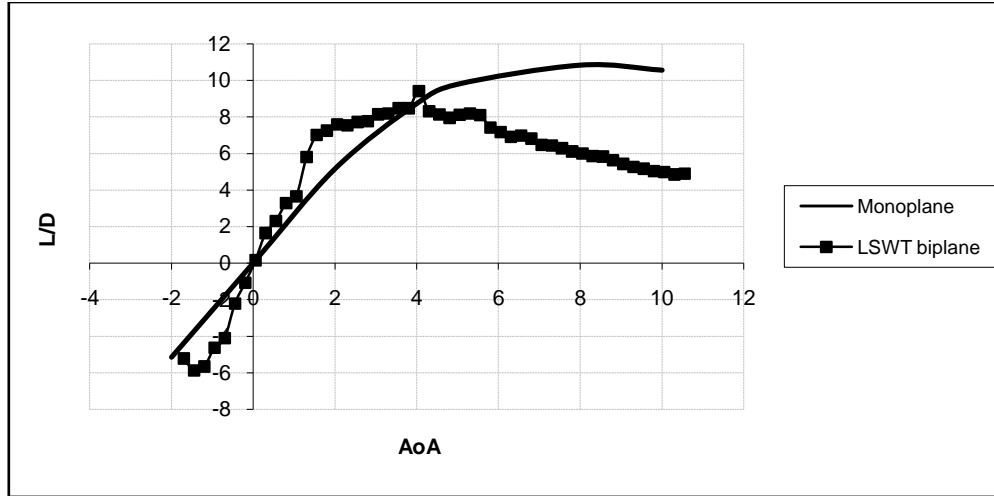


Figure 59 compares the aerodynamic efficiency of the biplane with endplates obtained from the UD-LSWT experimental data to the AVL results for the monoplane.

8 Conclusions

8.1 Flow Physics

- In contrast to inviscid computational results and Munk's theorem which predict no difference between positive and negative stagger, sharp differences in integrated lift were seen with positive stagger being consistently more efficient.
- Although viscous effects are likely responsible for the aforementioned behaviour, only minute differences in lift ($< 2\%$) were seen in varying Reynolds number from 60,000 to 120,000.
- Streamwise PIV shows that even though the upper and lower wings both have the same wing area, the upper wing always generates more lift, regardless of the stagger.
- Individual upper and lower wing downwash behaviour indicates that positive stagger significantly increases the lift efficiency of both the upper and lower wings, most likely due to the effects of the downwash of the upper wing on the lower wing and the associated change in effective angle of attack.
- Increasing gap always increases lift efficiency when stagger is negative.
- Increasing gap has reduced effectiveness as stagger increases positively.
- Streamwise PIV confirms that increasing gap increases lift efficiency through increased downwash angles.
- Increasing gap increases the upper wing and lower individual wing performance in a manner similar to increasing stagger.
- Wing downwash angle is a reliable manner to predict biplane lift at the Reynolds numbers tested at lower angles of attack (< 10 degrees).
- Arguments supporting a leading edge separation bubble are somewhat supported by the fact that for negative stagger (the cases with the greatest reduction in downwash) the 2-dimensional downwash predicted lift does not account for all of the lift measured by the force balance at angles of attack beyond 5 degrees.
- Kutta-Joukowski integration of circulation in the near wake of the biplane configurations joined at the tips by endplates compares quite well to lift measured by force balance for the zero and positive stagger cases, but does not compare well for the negative stagger cases at the higher angles of attack.
- For the aforementioned cases where integration of circulation in the region of the wingtip vortex did not agree well with the force balance results, it is suspected that some form of leading edge separation bubble was occurring that contributed to lift outside of the PIV field of view.

- Kutta-Joukowski integration of circulation in the near wake of the biplane configurations joined at the tips by endplates compares quite well to lift measured by force balance for the entire range of gap cases tested.
- A generalized empirical equation is proposed to determine the lift curve as a function of gap, stagger, and aspect ratio. This equation has been validated in wind tunnels outside of the UD-LSWT against configurations vastly different from those tested in the UD-LSWT.
- A “kink” or two discrete linear regions were discovered in biplane lift curves.
- The magnitude of the increase in lift curve slope after the region of transition is best correlated by the angle of stagger across the ranges of gap and stagger tested.
- The absence of non-linearity in the lift curve combined with the insensitivity to Reynolds number defies explanation as typical “viscous” behavior; however, results from inviscid codes and theory do not exhibit the “kink.”
- Both the equivalent monoplane and biplane theories predict the drag well up to the region of transition before the “kink.”
- 2-dimensional momentum deficit drag results agree well with the force balance drag predictions for the negative stagger cases, once again contradicting the logic behind the presence of any “extra” or vortex lift mechanisms since if they were in fact present, their associated drag would not be well measured by 2-dimensional momentum deficit methods.
- Downwash angle used to predict lift agrees well with the force balance data providing yet another contradiction to the posited explanation of vortex lift since vortex associated suction lift would also not show up as downwash [Newtonian] lift.
- The wake morphology and thus the lift induced drag are directly influenced by the gap, stagger and the presence, shape, and toe-in angle of the endplates.

8.2 Design

The following conclusions can be made about the design of this class of vehicle, assuming:

- An elliptical load distribution along the quarter chord
- A symmetrical lift distribution between the upper and the lower wing
- The same reference planform area between the nonplanar wing concept under investigation and the equivalent wing configuration
- The same total load
- The same structural material
- Uniform thickness along the span and the chord (for simplicity in modelling)

- The nonplanar wing concept under investigation can potentially meet some of the requirements of a Small Reconnaissance Surveillance and Target Acquisition UAV
- Light weight due to the potential reduction in structural weight
- Hand Launched due to the potential reduction of in stall speed
- Potential increased Endurance, using the same battery and motor
- Low visibility and portability due to the small size of the span in comparison to an equivalent monoplane with a span two times bigger.
- Using the finite element software ADINA, eight structural models with varying gap and stagger were created from the nonplanar wing concept under investigation. The model with 1c gap and 0 stagger has the smallest Maximum Effective Stress at the root. The stagger has a deteriorating effect on the structural behaviour of the wing while the gap and therefore the endplates at the tips of the wing have a beneficial structural effect.
- If the model with 1c gap and 0 stagger is compared to an equivalent biplane, under the above mentioned assumptions, a reduction of 32.03% in the maximum stress is achieved, with an increase in the weight of 13.5% due to the presence of the endplates.
- If the model with 1c gap and 0 stagger is compared to an equivalent monoplane, under the above assumptions and the further assumptions of the same AR, different span and the same maximum effective stress at the root, a potential weight saving of 30% is realized, with a reduction in the stall speed of 19% and an increase in the endurance 6.4%, using the same battery capacity and the same motor.
- Using the panel vortex code AVL a second equivalent monoplane model was created under inviscid, steady, incompressible and irrotational flow assumptions. If the model with 1c gap and 0 stagger is compared to this second equivalent monoplane, under the additional assumptions of the same span, different AR and the same maximum effective stress at the root, a potential weight saving of 3.5% is realized. From an aerodynamic point of view, an increase in the lift slope also results. Outside of small angles of attack, 0 thru 4°, Lift to Drag ratios which represent the aerodynamic efficiency of a range-optimized aircraft, are greater than those for the equivalent monoplane. In particular at the supposed design C_l for the proposed Small UAV mission, a gain in L/D of 17% is realized.

9 References

- [1] Fry, Timothy J., “Unique Stealth UAV Houck Aircraft Design Program, Vol. II: Prototype Report”
- [2] Walker, M., “The Aerodynamic Performance of the 24 inch Houck Configuration,” Master’s Thesis, U.S. Air Force Institute of Technology, Wright-Patterson AFB, OH, 2007.
- [3] Killian II, Dermot N., “The Aerodynamic Performance of The Houck Configuration Flow Guides,” Master’s Thesis, U.S. Air Force Institute of Technology, Wright-Patterson AFB, OH, 2007.
- [4] Oligney, B. and Frash, M., “Aerodynamic Evaluation and Optimization of the Houck Joined Wing Aircraft”, AIAA-2008-1422, 46th AIAA Aerospace Sciences Meeting and Exhibit, Reno, Nevada, 2008.
- [5] Barlow, Jewel, “Houck Configuration – Wind Tunnel Test Data Report,” Glenn L. Martin Wind Tunnel Test 1989, University of Maryland, Submitted to the USAF Research Laboratories Air Vehicles Directorate, May 2008.
- [6] Kang, Hantae, “Gap and Stagger Effects on the Aerodynamic Performance and Wake Behind a Biplane with Endplates,” Doctoral Dissertation, University of Dayton, Department of Mechanical and Aerospace Engineering, Dayton, OH, 2008.
- [7] Genco, N., “Parametric Study of the Performance of a Biplane Joined at the Tips,” Master’s Thesis, University of Dayton, Department of Mechanical and Aerospace Engineering, Dayton, OH, 2008.
- [8] Landolfo, Giuseppe, “Aerodynamic and Structural Design of a Small Nonplanar Wing UAV,” Master’s Thesis, University of Dayton, Department of Mechanical and Aerospace Engineering, Dayton, OH, 2008.

-
- [9] Betz, A., "Die gegenseitige Beeinflussung zweier Tragflächen," Z.F.M., Oct. 17, 1914, pp. 253-258.
- [10] Betz, A., "Berechnung der Luftkraftw auf eine Doppeldeckerzelle aus den entsprechenden Werten für Eindeckertragflächen," T.B., Vol. I, No. 4, 1917, pp. 103-107.
- [11] Fuchs, R., "Systematic Rechnung über Auftrieb und Widerstand beim Doppeldecker," T.B., Vol II, No. 2, pp. 177-185.
- [12] Fuchs, R., and Hopf, L., *Aerodynamik*. Richard Carl Schmidt & Co., 1922.
- [13] Diehl, Walter S., "Relative Loading on Biplane Wings," NACA Report-458, 1934.
- [14] Munk, M. M., "General Biplane Theory," NACA Technical Report TR-151, 1929.
- [15] Kroo, I. "Nonplanar Wing Concepts for Increased Aircraft Efficiency," VKI lecture series on Innovative Configurations and Advanced Concepts for Future Civil Aircraft, June 6-10, 2005.
- [16] Ahmed N., and Archer, R., "Performance Improvements of a Biplane with Endplates," Journal of Aircraft, Vol.38, No.2, 2001.
- [17] Munk, M. M., "The Minimum Induced Drag of Aerofoils," NACA Technical Report TR-121, 1923.
- [18] Prandtl, L., "Induced Drag of Multiplanes," NACA TN-182, 1924.
- [19] Knight, M and Noyes, R, "Wind Tunnel Pressure Distribution Tests on a Series of Biplane Wing Models", NACA-TN-310, 1929.
- [20] Barlow, J.B., Rae , W.H.R., Pope, A., *Low-Speed Wind Tunnel Testing*,

-
- [21] Logan, M., Chu, J., Motter, M., Carter, D., Ol, M., Zeune C., "Small UAV Research and Evolution in Long Endurance Electric Powered Vehicles," American Institute of Aeronautics and Astronautics, May 2007.
- [22] Naimer, N., Koretz, B., Putt, R., "Zinc-Air Batteries for UAVs and MAVs," www.electric-fuel.com/defense/UVS02.pdf.